Impact of biomass inorganic impurities on hard carbon properties and performance in Na-ion batteries

Adrian Beda, Jean-Marc Le Meins, Pierre-Louis Taberna, Patrice Simon, Camelia Matei Ghimbeu

Impact of biomass inorganic impurities on hard carbon properties and performance in Na-ion batteries

Adrian Beda [1,2], Jean-Marc Le Meins[1,2], Pierre-Louis Taberna [3,4], Patrice Simon [3,4], Camélia Matei Ghimbeu [1,2,4,*]

[1]Université de Haute-Alsace, CNRS, Institut de Science des Matériaux de Mulhouse (IS2M) UMR 7361, F-68100 Mulhouse, France

[2]Université de Strasbourg, F-67081 Strasbourg, France

[3]Université de Toulouse, CIRIMAT, UMR-CNRS 5085, F-31062 Toulouse, France

[4]Réseau sur le Stockage Electrochimique de l'Energie (RS2E), FR CNRS 3459, 80039 Amiens Cedex, France

∗Corresponding author at: Université de Haute-Alsace, CNRS, Institut de Science des Matériaux de Mulhouse (IS2M) UMR 7361, F-68100 Mulhouse, France.

Abstract

Biomass waste recently emerged as efficient precursors for hard carbon anode preparation for Na-ion batteries. Despite their very complex microstructure (organic/inorganic) there is a lack of knowledge about their impact on carbon formation. In this paper, the influence of inorganic impurities of three raw local biomass wastes (asparagus, grape and potato) on the hard carbon properties and on their electrochemical performance is investigated, by performing a washing step either before or after the thermal treatment (TT) at 1300 °C. When washing was done after the TT (with HCl), most of crystalline inorganic impurities (K, Ca, Si, Mg - based compounds) could be significantly removed. This triggered the increase of ultramicroporosity along with mesoporosity formation and graphite interlayer space (d_{002}) contraction. Such observations are less pronounced on grape derived carbon due to the inorganic's catalytic induced local graphitization during pyrolysis. The oxygen content in the pristine carbons was high, owing to the presence of inorganic metal oxides and carbonates, and could be diminished after washing along with the amount of defects. Thus, the carbon content and the electronic conductivity of the materials were enhanced. The electrochemical performance improvement after washing was limited since the positive effect brought by impurities removal was negatively compensated by the changes occurring in the materials, particularly the increase in the specific surface area. Diffrently, the washing done before the TT (with water) induced only fewer changes on the materials porosity and structure and slightly improved capacity (from 215 to 230 mAh g^{-1}). Furthermore, higher pyrolysis temperature (1400 °C) on washed HCs afforded a better reversible capacity up to 280 mAh g^{-1}. This comprehensive study opens the door for green and mild synthesis approach to be further explored for sustainable fabrication of hard carbon for Na-ion batteries.

Keywords: biomass waste; impurities; hard carbon; energy storage; Na-ion batteries.

GRAPHICAL ABSTRACT

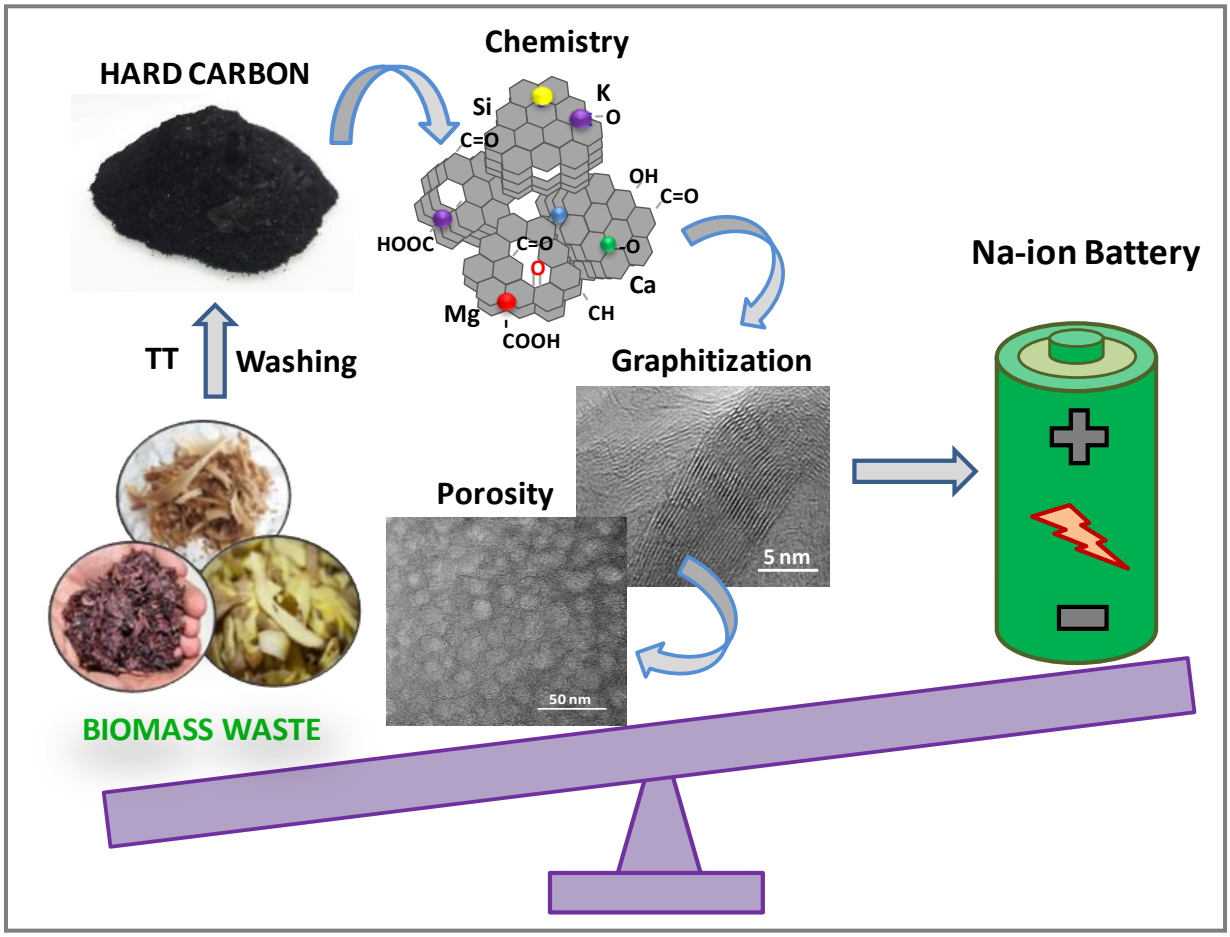

Biomass waste inorganic impurities impact the structure, the porosity and the surface chemistry of hard carbon and their performance as anode in Na-ion batteries.

1. INTRODUCTION

Lately, Na-ion batteries (NIBs) have gained more and more attention as the shortcomings of Li-ion batteries become increasingly evident: safety issues, high demand due to the fast development of electric vehicles, a possible depletion of Li resources, the political instability in the Democratic Republic of the Congo (leading exporter of cobalt, used for cathode preparation), etc. For the development of anode materials for NIBs, several materials have been explored [1]–[5], and among them hard carbon received greater attention due to its advantages such as low price, high availability, tunable features and theoretical capacity close to graphite. That is why a wide range of sources are used to develop hard carbons and involves numerous synthetic precursors (i.e., phenolic resin, polyacrylonitrile, polyaniline), bio-polymers (i.e., cellulose, sucrose, glucose, lignin) or biomass.

Biomass is one of the most abundant sources of renewable energy which originates from different wastes (urban, domestic, agriculture, forestry), trees, plants, algae, etc. Up to 15% of global energy demand is provided by biomass. Having a structure composed mostly from cellulose, hemicellulose and lignin (and low amounts of proteins, ash and pectin) and a composition rich in carbon that can exceed 60% (on a dry basis), biomass represents the most approached category of precursors to develop hard carbon anodes for sodium ion batteries [3], [6], [7]. Several literature studies reported hard carbon anodes based on a broad range of biomass precursors such as: fruit peels [8]–[12], different nuts shells [13]–[16], agro-industrial residues [17]–[19], pinecones [20], peat moss [21], algae [22], cellulose [23]–[25], lignin [26]–[28], sucrose [29], glucose [30]–[32], etc. It appears evident that the term biomass includes various precursors which can be subdivided in other categories such as: bio-waste (fruit/vegetable peels, agro-industrial residues), carbohydrates (sucrose, glucose) and biopolymers (lignin, cellulose). However, when selecting biomass precursors, some important aspects should be taken into consideration. First, the precursor should not be destinated for human's food purpose (i.e., fruits, sugar sources), reason why bio-waste represents a more suitable option. Another important aspect is the biomass chemical composition (including heteroatoms and inorganic elements) and the microstructure which is rather unique. These features have a significant influence on the final hard carbon properties (structure, texture, morphology and composition) and further on the delivered performance. Moreover, as the quantity of produced bio-waste increases continuously, exploring them represents a real advantage to reduce the waste by transforming them in high added-value hard carbon materials, for instance.

Generally, the synthesis of hard carbon involves only a pyrolysis step, yet, in several works the synthesis procedure implies an additional activation post-/pre-treatment [9], [12], [17], [33] or doping [34] stage, aimed to reach higher performance. However, very little or no attention is paid to the inorganic impurities contained in such hard carbon materials and there is no bottom line for all these studies involving rather trials on random precursors that can be turned into carbon. Moreover, there is no real correlation found so far between the materials features (i.e., interlayer distance, porosity, surface functionality) and the inorganic impurities presence. Some of the few approaches reported in the literature are discussed further. One of them involved the valorization of lignin as hard carbon anode [28]. Direct pyrolysis of lignin (1200°C) leaded to high surface area carbon due to *in-situ* activation induced by alkaline impurities and electrochemical capacity fading over cycling. For this reason, washing with water was performed after an intermediate carbonization step (600 °C) in order to remove the impurities (Na, K-based due to the extraction process in the paper industry) followed by pyrolysis at 1200 °C. As result, the N_2 specific surface area (SSA) decreased considerably (from 180 to ~10 m^2 g^{-1}), the d-spacing slightly diminished, as well, while the electrochemical performance was improved (both reversible capacity and stability over cycling). In another study, [35] chitosan precursor was washed after the heat treatment at 1300°C with an acidic solution (20% HCl) to remove the Ca-based impurities coming from its extraction from sea food shells. Although efficient, washing does not significantly alter the texture or structure of the hard carbon, but an increase in active surface area (ASA) could be observed (from 1.8 to 5.2 m^2 g^{-1}). Regarding the electrochemical performance, the washing rather improved the anode stability over cycling. Passerini and co-workers [36] studied the impact of acidic treatment on biomass derived hard carbons as well. Phosphoric acid was used to treat the peanut shells precursor for different periods of time (1 day, 6 days, or 2 weeks) leading to correlations between the treatment time and the structural properties / electrochemical performance. When the precursor was treated for a longer time, the obtained HC has a lower specific surface area and an improved structural organization. Consequently, the delivered reversible capacity improved as well, i.e., 120 mAh g^{-1} for 1 day to 290 mAh g^{-1} after 2 weeks of acidic treatment. In another work, hard carbon was obtained from argan shell [15] by performing different types of pre-carbonization washing steps: with acetone (followed by thermal annealing) and acetone followed by an acidic washing (2M HCl solution). Although the study focused more on the influence of the heat treatment temperature, it was observed that the washing carried out with HCl solution leads to a higher reversible capacity which was attributed to a larger number of active sites (defects and/or voids). Dupont *et al.* published a study aimed to elucidate the

influence of different biomass composition on hard carbon properties and electrochemical performance [37]. The authors concluded that the initial biomass composition and origin (wood *vs.* plant derived) has a greater effect on hard carbon properties than the used temperature range (1100-1400 °C). The wood derived HC lead to high carbon content possessing turbostratic structure and high reversible capacity while the plant derived HC resulted in lower reversible capacity due to a lower carbon content and higher impurity amount.

Therefore, although, the few existing works underline significant altering of carbon properties and performance due to impurities presence, none of them specifically addressed in a systematic way or purpose the impact of impurities on the carbon properties, electrode conductivity and electrochemical performance.

The aim of this paper is thus to provide more insights on the impact of biomass impurities on the obtained HCs properties as well as on their electrochemical performance, impact that seems rather important although very little knowledge exists so far. For this purpose, three types of precursors were selected for HC preparation: asparagus peel, grape waste or pomace (solid waste resulted from the activity of wine production) and potato peels. The selection is based on their great significance for Alsace region, France. Terefore, large scale production perspective was considered, in order to privilege precursors that satisfy availability issues from local waste resources, which is highly advantageous for production cycle life assessment.

A simple washing step (before or after the TT) was performed to elucidate how the carbon characteristics, (composition, structure, porosity, defects and electronic conductivity) modifies with impurities removal and how the electrochemical performance is further impacted. The obtained results herein revealed a significant amount of inorganic impurities in carbon structure, which, in some cases, are able to graphitize the carbon leading to different structure and amount of defects. Furthermore, it was found that the porosity increases while the amount of functional groups decreases when the impurities are removed. The carbon content and the electronic conductivity were greatly enhanced as well. The electrochemical performance was strongly affected by these changes and improvements were observed after impurities removal.

2. EXPERIMENTAL SECTION

2.1. Materials synthesis

Asparagus peel (A) and potato peel (P) were obtained as a result of personal consumption of the local products while the grape waste (G) originated from local wine production. The raw materials were first dried overnight at 80 °C to remove the excess of water, then a thermal

treatment was performed with a heating rate of 5 °C min^{-1} until 1300 °C, under Ar flow (15 L h^{-1}). The temperature was maintained for 1 h, and then the sample was naturally cooled down (Scheme 1, route 1). Before using, all the materials were grinded to have a fine and homogeneous powder. The obtained hard carbons (HCs) are further denoted "HC-X", where *X* is the used precursor (P-from potato, A-from asparagus and G-from grape). Two types of washing steps were conducted, *i.e.*, before and after pyrolysis step, as exposed in Scheme 1.

The hard carbons washed after (*wa*) the TT (route 2) where obtained as follows: once annealed at 1300 °C, the carbon samples were first mechanically stirred with a solution of HCl (18.5%). Next, the hard carbon powder was recovered by filtration, followed by washing with distilled water in abundance (500–700 mL) to remove the excess of HCl and to achieve a neutral pH - equal to 6.5–7). The samples were then dried at 80 °C overnight, and grinded before analyses. The samples are denoted HC-Xwa.

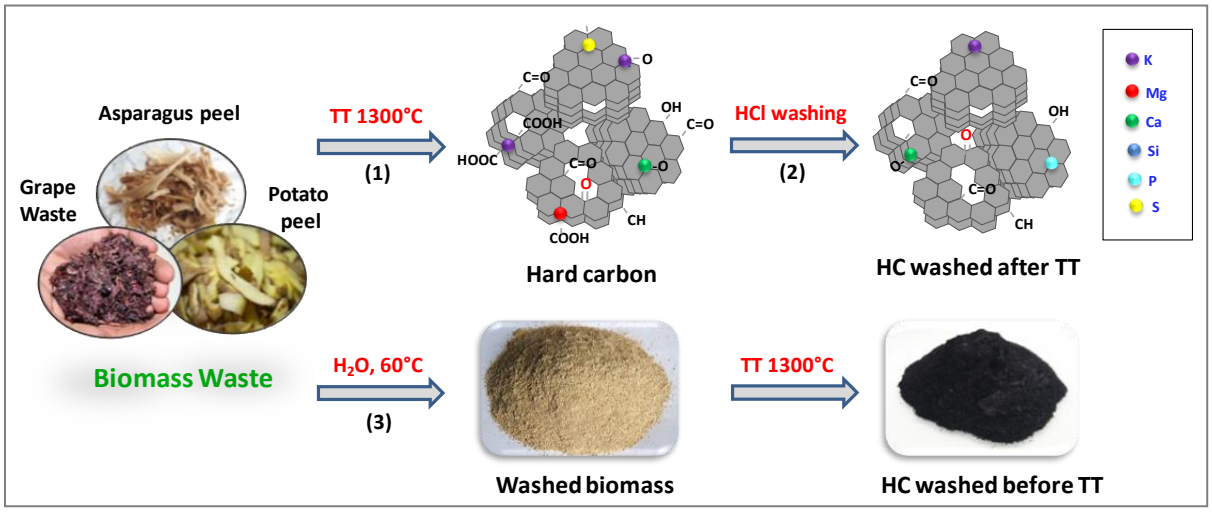

Scheme 1. Synthesis routes used to prepare hard carbons derived from raw biomass precursors: (1) pristine HC, (2) HC washed after the TT, (3) HC washed before the TT.

The precursors washing before (*wb*) the heat-treatment was done to evaluate the efficiency in removing the impurities (route 3, Scheme1). The raw biomass was stirred with distilled water at 60 °C overnight, then recovered by filtration (washed with excess of water) and dried at 80 °C before the heat treatment at 1300 °C. Worth to mention, that no HCl was used in this case in order to avoid biomass modification. The samples are denoted HC-Xwb.

2.2. Material characterization

The biomass weight loss and its conversion into carbon during the thermal pyrolysis was performed by thermogravimetric analysis (TGA) with a Mettler-Toledo TGA 851e by heating the biomass to 900 °C with 5 °C min^{-1} heating rate under N_2 atmosphere. The amount of inorganic impurities present in the carbon materials composition was determined as well, by performing a TGA measurement under air, up to 950 °C (5 °C min^{-1}). The chemical composition was assessed by Energy-dispersive X-ray spectroscopy (EDX) using a JED 2300 detector attached to a FEI Quanta 400 scanning electron microscope. The structure of the hard carbon materials was studied by several techniques. High-resolution transmission electron microscopy (HRTEM) was done with a JEOL ARM-200F instrument operating at 200 kV. Raman spectroscopy was performed at room temperature using a LabRAM BX40 (Horiba Jobin-Yvon) spectrometer equipped with a He–Ne excitation source (532 nm wavelength). For accurate analysis, several spectra were acquired (mapping) and the average spectrum was used. X-ray diffraction (XRD) analysis was performed using a Bruker D8 Advanced diffractometer with Bragg-Brentano θ-θ geometry equipped with a LynxEye XE-T high resolution energy dispersive 1-D detector (Cu $K\alpha_{1,2}$).

Textural properties of the hard carbon materials were investigated with a Micromeritics ASAP 2420 machine using N_2 gas as adsorbate (77 K) and a Micromeritics ASAP 2020 instrument using CO_2 adsorbate (273 K). In an initial step, the samples were outgassed for 12 h at 300 °C, under vacuum in the degassing port and for another 2 h on the analysis port to remove any trace of molecules. The Brunauer-Emmett-Teller (BET) specific surface area (SSA) was determined from the linear plot in the relative pressure range 0.05–0.3 and 0.01–0.03 for N_2 and CO_2, respectively. The pore size distribution (PSD) was obtained from N_2/CO_2 adsorption isotherms using the non-local density functional theory (NLDFT) considering the standard slit pore model for carbon materials carried out by SAIEUS software (Micromeritics).

Temperature-programmed desorption (TPD) analysis was used to determine the nature and the amount of oxygen-based functional groups present in the materials and to quantify the amount of defects in terms of active surface area (ASA). Thus, the measurements were performed in a vacuum system equipped with a mass spectrometer (MS) that was constructed in the laboratory [38]. A small amount of carbon (~7 mg) was heat-treated up to 950 °C at a heating rate of 5 °C min^{-1}. The gases released were quantitatively analyzed during the experiment by the mass spectrometer which was calibrated regularly, using several gases usually desorbed from the

carbon surface. Prior to each analysis, a N_2 sensibility measurement was performed, which allowed further quantification of the other gases. To determine the ASA, the materials were exposed to oxygen introduced at 300 °C (oxygen pressure: 66.5 Pa), which was subsequently chemisorbed for 10 h to form surface oxygenated complexes. A second TPD was performed at 950 °C with a 10 °C min^{-1} heating rate to determine the amount of oxygenated groups, and finally the ASA considering that the area of an edge carbon site that chemisorbs an oxygen atom is 0.083 nm^2.

2.3. Materials electro-chemical characterization

The electrochemical tests were performed using two electrodes Swagelok cells. For electrode preparation, the hard carbons were mixed with polyvinylidene fluoride (PVdF) binder and carbon black acetylene conductive additive (mass ratio of 70:10:20) in presence of *N*-methyl-2-pyrrolidone (NMP) as solvent. The obtained slurry was coated by doctor blade on Al foil. Electrodes with a mass loading of 2–3 mg cm^{-2} (12 mm diameter) were first dried at 80 °C under vacuum before testing.

The HC conductivity was evaluated with the help of EIS (Electrochemical Impedance Spectroscopy). The electrical resistance of the electrodes was measured, then the electrical conductivity was calculated based on the following formula:

$$\sigma = \frac{L}{RA} \qquad (1)$$

where, (σ) – electronic conductivity, (L) – electrode length, (R) - electrical resistance and (A) - sectional area of the HC electrode.

The cells were assembled in an argon-filled glove box using sodium metal as counter/reference electrode and a glass fiber separator. The electrolyte consisted of 1 M $NaPF_6$ dissolved in ethylene carbonate (EC)/ dimethyl carbonate (DMC) with a 1:1 volume ratio. The electrochemical performance was measured using a Bio-Logic cycling device. Galvanostatic charge-discharge tests were conducted at a constant current in a voltage window between 0.01 and 2 V (vs. Na^+/Na) at C/10 rate (the theoretical specific capacity was considered 372 mAh g^{-1}). At the end of each discharge and charge cycle, potentiostatic steps with a duration of 1 h were added. Cyclic voltammetry was performed in the voltage window 0.01–2 V at scan rates of 0.2 mV s^{-1}. All experiments were conducted at room temperature and the potentials are expressed relative to Na metal (*vs.* Na^+/Na).

3. RESULTS AND DISCUSSION

3.1. Biomass conversion and carbon composition

The hard carbon materials derived from biomass wastes were characterized to elucidate the presence of impurities in their structure and to evaluate their performance in sodium storage applications. In a first step, TGA/DTG measurements were performed on the raw biomass samples to understand their thermal conversion into carbon, as well as to determine their final carbon yield after pyrolysis.

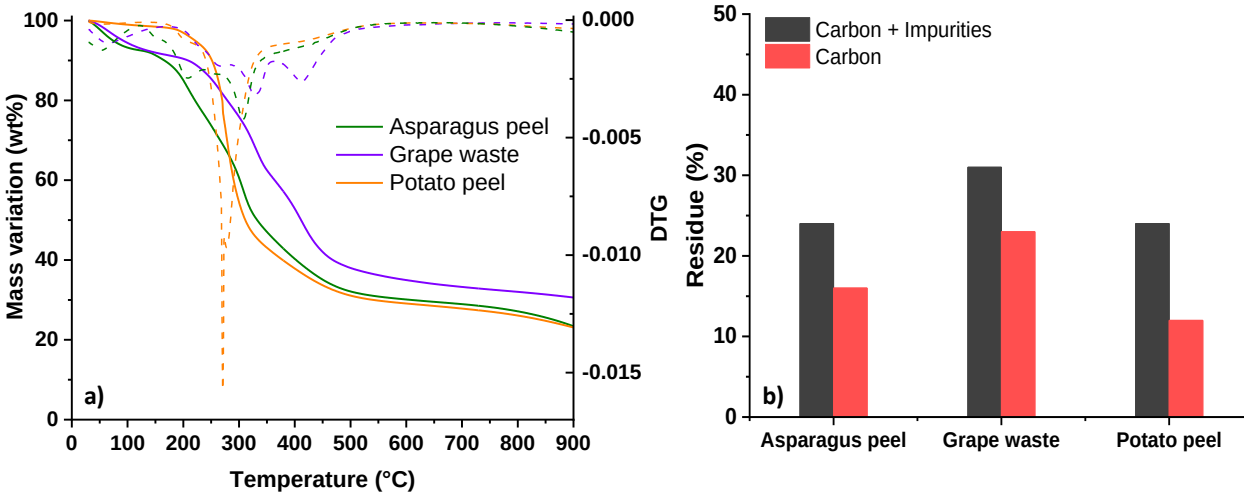

Figure 1. a) TGA/DTG curves under nitrogen of the different biomasses; b) Residue yield obtained from the raw biomass conversion into carbon at 900°C and the carbon yield obtained by subtracting the amount of impurities obtained following materials oxidation under air by TGA.

It can be seen in Fig. 1a that potato peel is very stable up to 200 °C as almost no mass loss occurs. On the other hand, asparagus and grape waste already lose apx. 10% of the mass until 200 °C due to the release of adsorbed water, although initially all materials were dried at 80 °C to remove the excess. In the temperature range 250–450 °C, a significant mass loss of apx. 60% occurs which is very sudden in the case of potato waste as suggested by the sharp and pronounced observed peak, in the DTG plot at ~270 °C. For a temperature higher than 300 °C, grape waste has a better thermal stability than the other two materials. The important mass loss observed for the three materials could be correlated to the decomposition of the main precursor constituents. In the case of asparagus peel, cellulose (decomposes between 260 and 350 °C [39]) and hemicellulose (200–280 °C [39]), are the main constituents. Potato peel has a high content of starch (250–300 °C [40]) while the grape waste is rich in lignin (280–500 °C [39]), ~44% [41], but has also cellulose in its composition.

Although most of these biopolymers decompose in the same temperature range, 250–500 °C, lignin has a higher thermal stability (contains stable aromatic molecules) [42] which gives grape waste a better stability, higher cross-linking and thus a higher apparently C yield of 31 wt%, while asparagus and potato peel give a yield of 23 wt% (Fig. 1b, black bar). The impurities present in materials composition should be considered, as well, since they are stable at such temperatures and contributes to the final residue mass of the obtained material. Therefore, the observed yield is not only related to carbon but also to the inorganic part. To check this aspect, EDX was implied to determine the composition of biomass precursors and the results are shown in Table S1 (Supporting Information) and Fig. 2.

A high weight percentage of oxygen can be seen in the biomass precursors structure (43–52 wt%). An important amount of K along with Ca, P, Si, S, Mg or trace of Cl were found in the composition of the materials, as well. However, the quantity of impurities seen for grape waste is not very high to justify its higher residue yield after pyrolysis. A contribution may come from the carbon content in the biomass, which is higher in the case of grape waste (54 wt%) compared to the other precursors (48 wt% for asparagus peel and 41 wt% potato peel). However, it is worth to mention that EDX does not take into account and/or underestimates the heteroatoms (*i.e.*, H, N, S) and thus complementary studies were performed by combustion elemental analysis (EA) to further elucidate the elemental composition (Table S2, SI). The results revealed a high amount of heteroatoms (N, H, S), *i.e.*, 10.5 wt% for asparagus peel, 8.7 wt% for grape waste and 8.3 wt% for potato peel.

Now if we compare the carbon % revealed by the two techniques, it can be noticed that the higher amount of heteroatoms (revealed by EA), present in biomass composition, led to an overestimation of carbon content by EDX (*i.e.*, 43.4 wt% by EA *vs*. 48 wt% by EDX for asparagus peel) but the trend between the materials is similar. On the other hand, the impurities (K, Ca, Si, etc.) and the oxygen cannot be quantified by EA and therefore, the two techniques are complementary and are both required to evaluate materials composition.

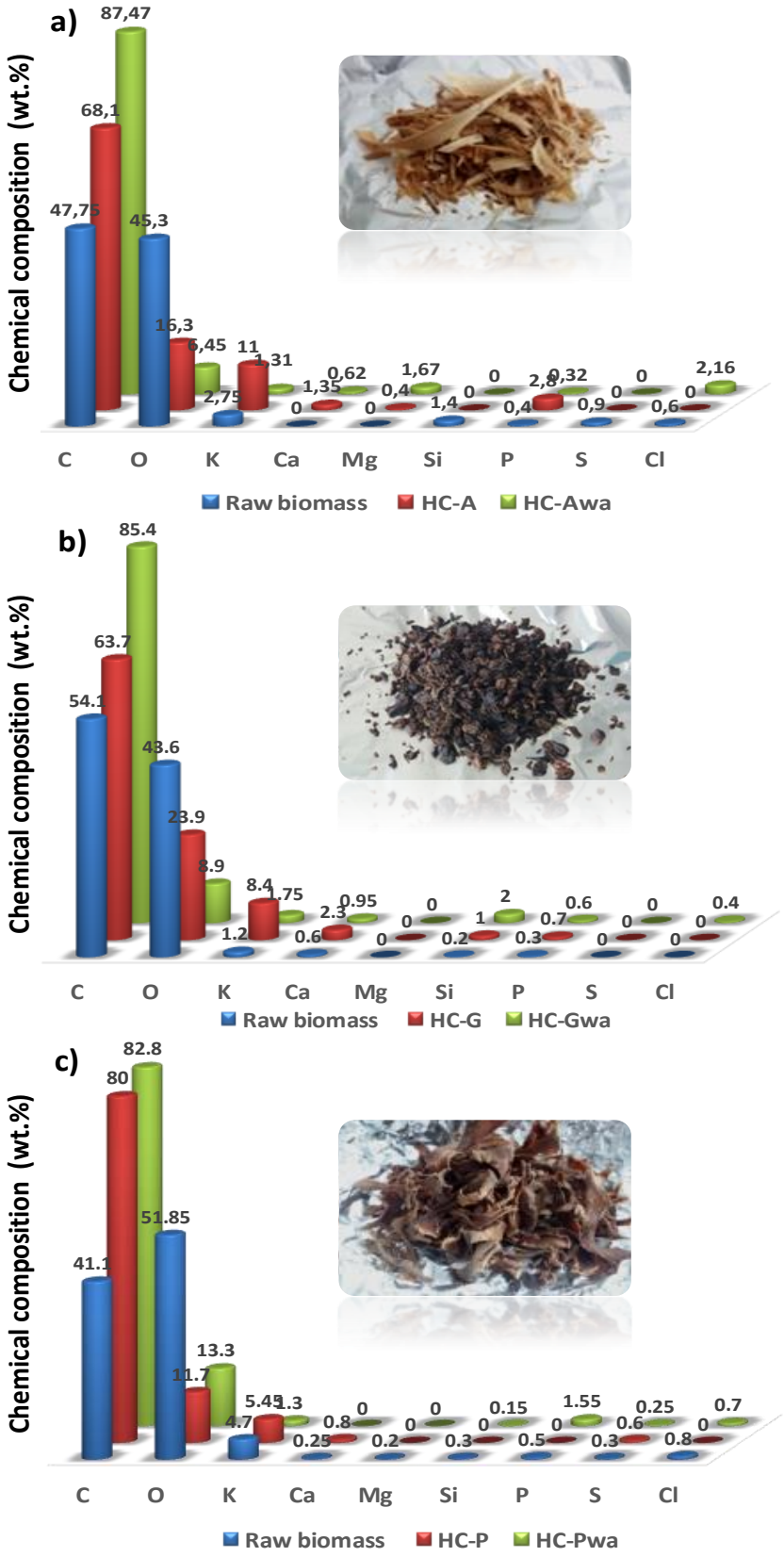

Figure 2. Chemical composition determined by EDX for biomass precursors, hard carbons and washed hard carbons after pyrolysis: a) asparagus, b) grape and c) potato. *In-set*: images of raw biomass precursors.

To elucidate the exact carbon yield in the materials, TGA was performed up to 950 °C on the hard carbon materials under air. This strategy was implied since the carbon burns at around 400–600 °C while the impurities have a higher thermal stability and can be quantified. Thus, the carbon was oxidized and removed as volatile gases (COx) and only the impurities remained but, worth mentioning, they are oxidized. The results (Fig. S1a, SI) confirm indeed the presence of apx. 10% residue which can be seen very well in Fig. S1c, SI, showing the crucibles recovered after the TGA analysis. By substracting the initial residue yield and the percentage of impurities, the real carbon yield was roughly estimated as shown in Fig. 1b (red bar). It can be noted that asparagus peels give 15 wt% yield in carbon, grape waste 23 wt% while potato peels only 12 wt%. Therefore, the higher carbon yield of grape waste is rather correlated to the amount of carbon in the precursor and its aromatic structure given by lignin, known to induce higher carbon yields [28]. The recovered residue powder was further analyzed by XRD (Fig. S1d, SI) and a complex mixture of mineral phases containing carbonates, silicates and phosphates ($CaCO_3$, K_2CO_3, $Ca_3(PO_4)_2$, $CaSi_2O_5$, etc.) could be identified. Thus, it can be concluded that the identified impurities justify the higher residue yield observed for the three precursors. Therefore, the yield in such materials is related to both carbon and the impurities.

3.2. Hard Carbon Structural characterization

Complementary techniques were used, to study the materials structure, *i.e.*, XRD, Raman spectroscopy and TEM techniques. In Fig. 3a, b, XRD diffractograms of pristine hard carbons obtained at 1300 °C along with their corresponding hard carbons washed after (wa) TT, are presented. The characteristic peaks of the hard carbon are seen for all three materials at a 2-theta position of ~23°, 43.8° and 80°, respectively. However, it seemed important to proceed with discernment on the exact position of the (002) line, characteristic of the graphene interlayer space (d_{002}). One of the difficulties lies in the presence of numerous impurities in the HC materials, which hamper the correct estimation of the (002) peak position. Conventional tools for simple determination of reflection positions available in all search-match software may be insufficient. Specific attention was accorded to the background determination, in order to get a right description of (002) peak profile. The resulting data were converted via PowDLL [43] and then treated with the profile peaks fitting option in Winplotr [44]. The refined peaks positions led to calculated d-spacing for the pristine materials of 3.819(13) Å for HC-A, 3.788(7) Å for HC-G and 3.977(15) Å for HC-P, values wide enough to allow Na^+ insertion-extraction, as reported in literature [35,45].

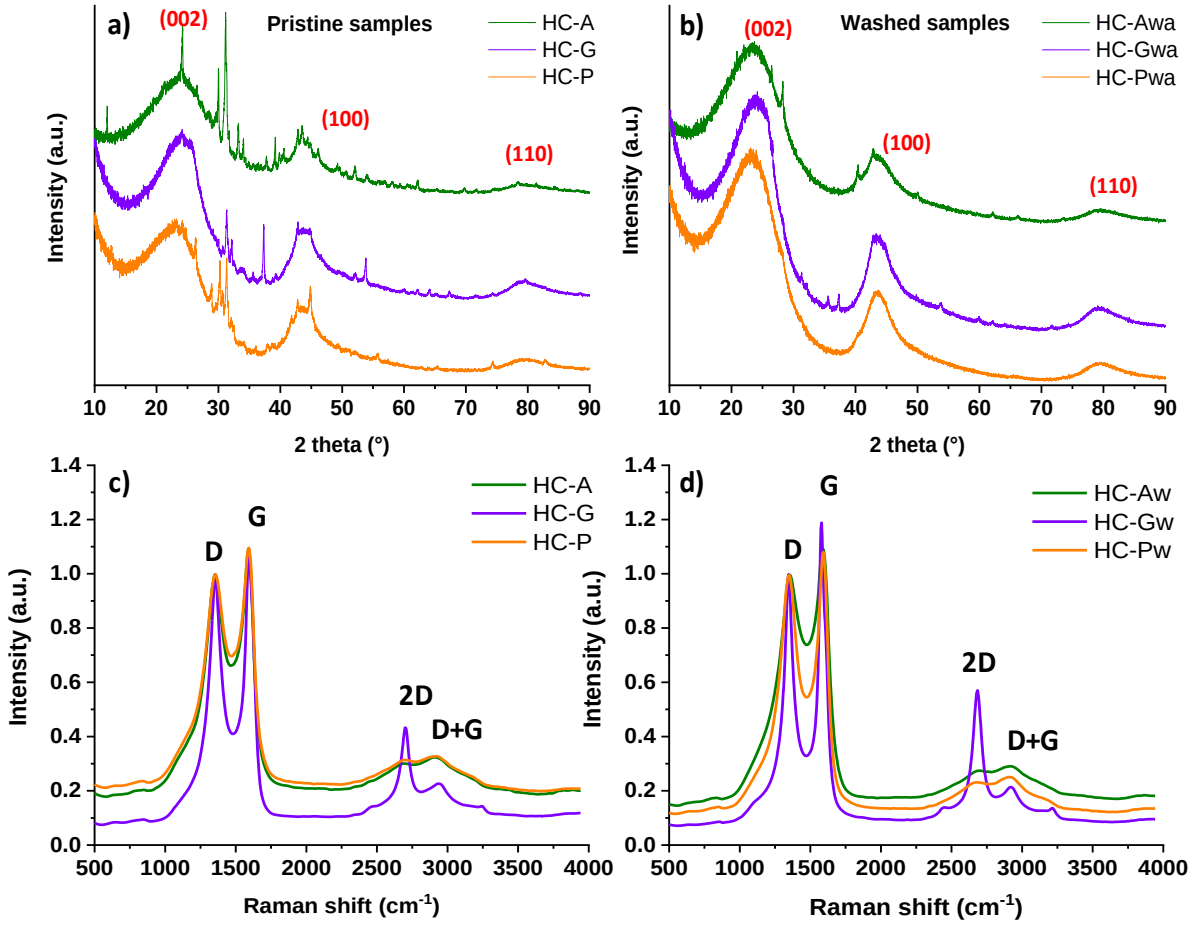

Figure 3. XRD diffractogram of (a) HC materials heat-treated at 1300°C along with b) washed after TT hard carbon materials. Raman spectra normalized to D band intensity of pristine (c) and washed (d) biomass derived hard carbons.

The presence of impurities is indicated by several sharp peaks visibles for all three pristine materials (Fig. 3a). The impurities identification based on XRD was rather difficult due to phase complexity, reason why it was assisted by EDX which was used to determine HCs composition. EDX results after pyrolysis (Fig. 2 and Table S3, SI) showed that the C content increases and reaches 80 wt% for HC-P, 68 wt% for HC-A while HC-G, has the lowest carbon percentage, ~64 wt%. Overall, these values are significantly lower than other hard carbons originating from lignin [28] or chitosan [35]. Moreover, the O content significantly decreases after pyrolysis, but for HC-G is still high, ~24 wt% compared to the other carbons (16.3 wt% for HC-A and 11.7 wt% for HC-P). A possible explanation could be related to the high amount of K and Ca contained in the structure which trap O_2 and induce the formation of carbonates. It is also clear from the obtained results that the amount of impurities in the carbon structure (*i.e.*, K, Ca, P, Si, S, Mg), is much higher after the heat-treatment compared to their parent precursors (31.9

wt% for HC-A, 36.3 wt% for HC-G and 18.5 wt% for HC-P). This can be attributed to the thermal decomposition of organic matter leading to a higher concentration of metallic impurities in the structure, following the thermal treatment. It can also be assumed that at such high temperature, the metals are already in vapor state and migrate towards the material surface. It was reported before that such impurities react with the O_2 and CO_2 from the atmosphere, while exposed to air, forming metallic oxides and/or metallic carbonates [28], which may also explain the large amount of oxygen. Such impurities (metals + heteroatoms) may have different negative impacts on the electrochemical performance such as a decrease of the overall material conductivity or electrolyte decomposition with formation of SEI layer causing an initial irreversibility and/or fading capacity, as reported before [28,35].

Considering the chemical composition revealed by EDX and with the help of XRD data processing software, it was possible to identify different metal oxides, metal carbonates and/or different complex phases as exposed in Table 1.

Table 1. The impurities identified in the HC structure with the help of DIFRAC.EVA software [46] based on XRD data (Crystallography Open Database: REV212673 2018.12.20, [47]).

Sample	Identified phases
HC-A	MgO; K_2O; K_2CO_3; $MgCO_3$; $K_2Ca(CO_3)_2$; $MgCaOCO_3$; K_3P
HC-G	$CaCO_3$; CaS; K_2SO_4; $K_2(CO_3)$; $K_2Ca(CO_3)_2$; K_2O; K_2SO_3
HC-P	CaO; K_2O; SiC; $Ca_3(PO_4)_2$; Ca_5P_8

In order to study the influence of impurities, the carbons were washed after the thermal treatment and the samples were analyzed again and are further discussed, in parallel. The XRD data show that the crystalline impurities have been largely removed after washing, however, few local small peaks are still noticed in the case of HC-Pwa and HC-Gwa (Fig. 3b). According to the same XRD peak profile refinement applied for the pristine HCs, the resulting interplanar distances $d_{(002)}$ of the washed HCs decrease for HC-Awa down to 3.766(7) Å (−1.4%), for HC-Pwa to 3.870(9) Å (−2.7%) and remains rather constant (inside estimated standard deviation) for HC-Gwa, *i.e.* 3.792(6) Å *vs.* 3.788(7) Å for HC-G.

This decrease in the interlayer distance after washing can be correlated to the removal of impurities, including ions inserted between the graphene planes. However, this phenomenon is less observed for HC-G and HC-Gwa, as washing has no particular effect on the $d_{(002)}$ value.

This decrease in the interlayer distance after washing can be correlated to the removal of impurities, including ions inserted between the graphene planes. However, this phenomenon is less observed for HC-G and HC-Gwa, as washing has no particular effect on the $d_{(002)}$ value. This observation can be correlated with the results of Raman measurements which show for this family of HCs a rather strong local graphitization. This graphitization confirmed by TEM can be at the origin of a disturbance for the mobility of ions between the graphite planes, which remain trapped.

TGA analysis, performed under air, on the washed hard carbons confirm that impurities removal was almost complete, especially in the case of HC-Awa and HC-Pwa for which almost empty crucibles were observed (Fig. S1c). The low percentage of residue found (2–3 wt%) may be caused by the formation of a possible crystalline phase (*i.e.*, Si, SiC) which cannot be removed from the structure by HCl washing. The removal of most of the impurities was also confirmed by the EDX analysis performed on the washed samples (Fig. 2 and Table S3, SI). A significant increase in the carbon content was seen, especially for HC-Gwa and HC-Awa, reaching 85.4 wt% and 87.5 wt%, respectively (*vs.* 63.7 wt% and 68.2 wt% before washing). In the case of HC-P, the percentage increased from 80 wt% to 88.4 wt% after washing. In the same time, the amount of oxygen decreases, since less impurities such as oxides/carbonates are present in the structure. Overall, most of the impurities were removed thus allowing to elucidate their influence on the carbon characteristics and Na^+ storage mechanisms, as presented later on.

Additional information about the materials structure, especially on the disorder degree, important feature for sodium storage, were obtained with the help of Raman analysis. The specific "footprint" of hard carbons is observed for all materials in the 1300–1700 cm^{-1} region, namely the defect induced D-band (1346 cm^{-1}) and the crystalline graphite G band (1585 cm^{-1}). Supplementary low intensity bands, 2D and D + G could be observed at higher Raman shifts (>2500 cm^{-1}). A high degree of graphitization is seen for HC-G (both pristine and washed), which is indicated by the intense and sharp 2D peak (Fig. 3c, d). Moreover, as the spectra were normalized to D band, they revealed a slightly higher intensity of G band (graphite) for the grape than both asparagus and potato peel HCs. Worth to note also that both G and D bands are much narrower for HC-G, which denotes a lower full width at half maximum (FWHM) than that of HC-A and HC-P (Table S4, SI). All these observations, leads to the conclusion that the HC-G is more graphitized than the other HCs, in line with the lower I_D/I_G and $FWHM_D/FWHM_G$ ratios. In fact, we reached the same conclusion by Raman mapping which

scans and analyzes a certain area and not only a local point (Fig. S2, SI.). It is important to note, however, that graphitization is local and not uniform in the structure (2D intensity varies), sustained also by the XRD data showing no intense 002 graphite peak but large hard carbon specific peak. After washing, the disorder degree (I_D/I_G) decreases for asparagus HC from 2.9 to 2.2, for HC-Gwa from 1.5 to 1.3 while for HC-Pwa from 2.5 to 2.0, in the same trend as impurities removal.

HR-TEM analysis was further used to elucidate the local structure of the materials as illustrated by the images of pristine/washed materials shown in Fig. 4.

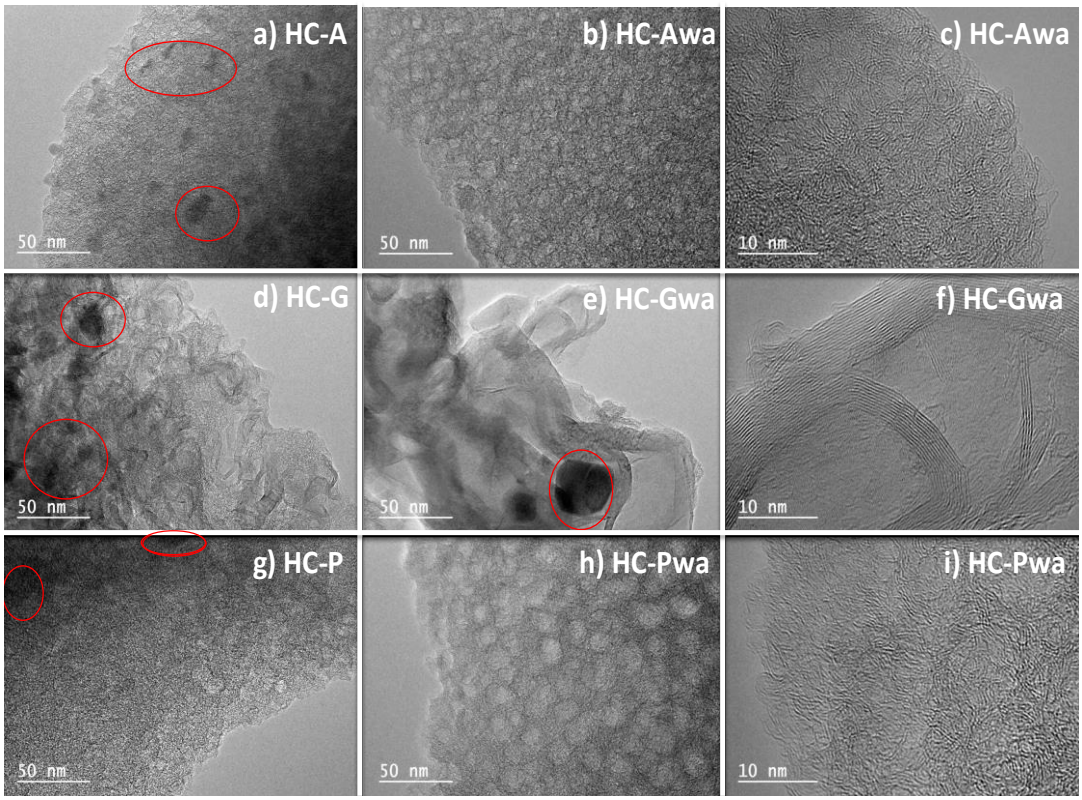

Figure 4. HR-TEM images of pristine and washed after TT hard carbons at different resolutions. The red circles highlight the presence of metal-based impurities.

The presence of impurities is highlighted by the black areas that largely disappear after washing. In the case of grape waste derived HC however, some large particles that are encapsulated in the carbon structure could not be removed by washing. The Si found in higher percentage in this material could be responsible for the higher graphitization degree found for HC-G. It may act as catalyst at elevated temperatures inducing structural graphitization [48]. The HR-TEM results are in good agreement with the XRD and Raman founding's: HC-Awa (Fig. 4c) and HC-Pwa (Fig. 4i) have a highly disordered structure with few local graphene stacked together while HC-Gwa (Fig. 4f) has a high degree of graphitization involving several stacked graphene layers (15–25). Despite the high degree of graphitization showed here, it is important to remind that TEM is a local technique, many areas on the material revealing a high disorder degree, similar to the one observed for HC-Awa and HC-Pwa samples, as illustrated in Fig. S3, S.I. Therefore, a heterogeneous structure combining mainly disorder carbon but also graphitic large domains is determined, in line with the Raman observations. It is worth mentioning that the local graphitization observed can have a negative influence on sodium ions storage either by limiting their intercalation between such graphitic layers with low d-space or by causing an irreversible insertion that could decrease the initial Coulombic Efficiency (iCE). An interesting aspect observed for the HC-Awa and HC-Pwa samples (Fig. 4b, h) is the structural pattern that involves some spherical white spaces (~10 nm diameter) that resemble to some extent with a well-developed mesoporosity. It is interesting that such mesopores were not observed for the pristine samples (Fig. 4a, g) and thus can be an indication that such impurities are located in the carbon structure and, as result of the washing step, they are removed deblocking some pores. Textural analysis might give more insights into this aspect.

3.3. Hard Carbon textural characterization

N_2 adsorption-desorption and CO_2 adsorption were used to characterize the hard carbons porosity. The pristine and washed after TT materials were studied in parallel to see if the presence of impurities can influence the textural properties (Fig. 5). Type II N_2 adsorption/desorption isotherms could be seen in the case of pristine hard carbons, which are specific for non-porous materials (Fig. 5a). The low amount of adsorbed N_2 by the materials atlow relative pressure (P/P_0) indicate limited amount of micropores (<2 nm).

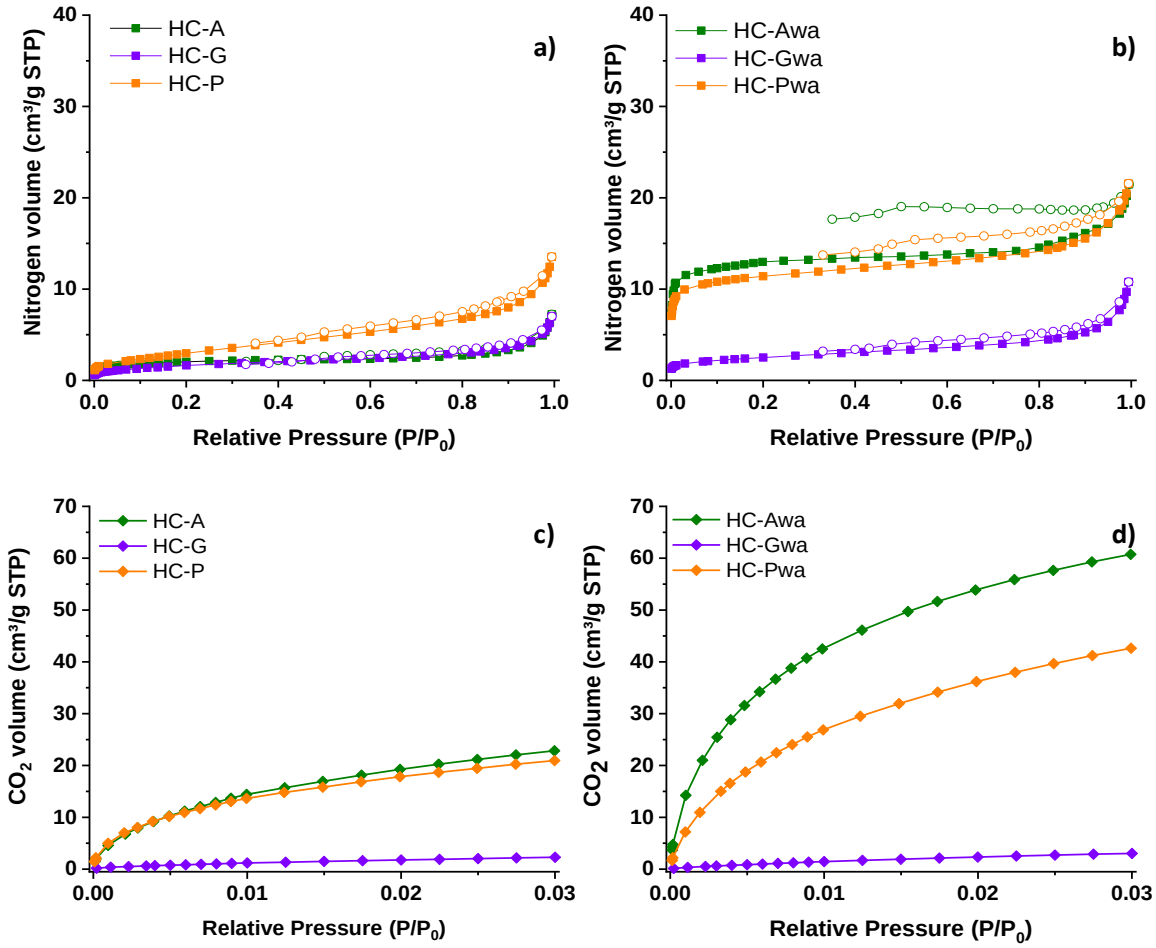

Figure 5. N_2 adsorption-desorption isotherms (a, b) and CO_2 adsorption isotherms (c, d) of pristine (left) and washed (right) HCs

For the washed materials, type II isotherms are kept for HC-Gwa while for HC-Awa and HC-Pwa a change of isotherms from type II to type IV occured. Such IV-type isotherms are characterized by an increased nitrogen adsorbed volume at low relative pressure and by the presence of a hysteresis loop at higher relative pressures, being specific for materials containing both micropores and mesopores. These observations are in agreement with the TEM results showing the presence of mesopores after impurities removal, for both HC-Awa and HC-Pwa. The SSA determined using the BET model is small for the pristine materials: 7 $m^2\ g^{-1}$ for HC-A, 6 $m^2\ g^{-1}$ for HC-G and 11.5 $m^2\ g^{-1}$ for HC-P, respectively (Table 2). On the other hand, the washed materials adsorb a much higher amount of N_2, which implicitly leads to higher SSA. This is especially observed for the HC derived from asparagus peels (40 $m^2\ g^{-1}$) and potato peels (35 $m^2\ g^{-1}$) while for HC-Gwa the specific surface increase is less significant after washing, (8.5 $m^2\ g^{-1}$).

Table 2. Hard carbon characteristics including, interlayer distance (d_{002}), disorder degree (I_D/I_G), specific surface area (N_2 and CO_2 SSA), oxygen-containing surface groups (CO_x), structural defects (ASA) and ASA/SSA.

Precursor	d_{002} (Å)	I_D/I_G	N_2 SSA ($m^2\ g^{-1}$)	CO_2 SSA ($m^2\ g^{-1}$)	CO_x (mmol g^{-1})	ASA ($m^2\ g^{-1}$)	ASA/SSA
HC-A	3.82	2.9	7	140	1.48	34.4	4.9
HC-Awa	3.76	2.2	40	334	1.30	44.8	1.1
HC-G	3.79	1.5	6	19	0.22	16.0	2.6
HC-Gwa	3.79	1.3	8.5	28	0.21	13.5	1.6
HC-P	3.98	2.5	11.5	127	2.22	52.6	4.5
HC-Pwa	3.87	2.0	35	265	1.13	43.3	1.2
HC-Pwb	3.93	1.9	9	103	0.72	11.5	1.2

With the removal of impurities from the structure, free spaces are created, recognized as porosity, thus explaining the observed changes. However, in the case of grape waste derived hard carbon, the limited SSA increase observed after washing (HC-Gwa) is unexpected considering the high amount of removed impurities revealed by EDX. Two effects can be proposed to explain this behavior. Indeed, most of the impurities placed at the surface are removed (confirmed by EDX results) leading to a certain porosity increase but part of the impurities catalyzed the carbon structure leading to graphitized areas. Therefore, while pore closure and d-spacing contraction occurs during pyrolysis, some impurities are encapsulated. Such particles are well confined in carbon, surrounded by graphitic shells which make them impermeable to acid, therefore, cannot be leached.

Pore size distribution (Fig. S4, SI) revealed that the materials possess mainly micropores (<2 nm) along with some mesopores (*i.e.*, 2–4 nm diameter). A small total pore volume could be determined as well, i.e., 0.01 $cm^3\ g^{-1}$ for HC-A and HC-G while for HC-P, 0.02 $cm^3\ g^{-1}$. After washing, impurities removal resulted in the significant increase of the micropore volume (i.e., 10 times higher for HC-Awa and 8 times higher for HC-Pwa). The PSD is better defined and pore size centered at 1 nm are seen.

As has been well pointed out before, HC texture does not involve only micropores and mesopores, a significant amount of ultramicropores (<0.7 nm) is also developed in the materials which are not detected by N_2 reason why, CO_2 adsorption must be implied. The adsorption isotherms of the pristine and washed materials are shown in Fig. 5c, d. The obtained results confirm the presence of ultramicropores (0.35–0.8 nm as evidenced by the PSD, Fig. S5, SI) leading to a significantly higher SSA for HC-A (140 $m^2 g^{-1}$) and HC-P (127 $m^2 g^{-1}$), respectively. In the case of HC-G, however, a small value is obtained once more, 19 $m^2 g^{-1}$, which indicates that the material structure is very compact with very little porosity developed. The same trend was observed when washing is done, SSA reaching a value of only 28 $m^2 g^{-1}$ for HC-Gwa while, in the case of HC-Awa and HC-Pwa, significant increase of BET SSA is observed to 334 $m^2 g^{-1}$ for HC-Awa and to 265 $m^2 g^{-1}$ for HC-Pwa, respectively (Table 2). The volume of ultramicropores (diameter centered at 0.5 nm) increases as well.

The obtained textural results reveal that the washing step causes the increase of both specific surface area and pore volume and the appearance of mesopores. Therefore, a network of pores involving meso-, micro- and ultra-micropores are present in the materials structure. However, in the case of grape waste derived HC, the material is rather non-porous which could to some extent limit sodium ions storage but in the same time might reduce undesired side reactions with the electrolyte (SEI formation).

3.4. Hard Carbon surface chemistry/defects

The EDX results presented in Fig. 2 pointed out a high content of oxygen in the HC structure. The oxygen is partially linked to the carbon structure forming oxygenated functional groups (carboxyl, carbonyl, ether…) while partially is bonded with the metallic impurities, forming oxides and carbonates (based on XRD). To obtain more insights about the materials surface chemistry (functional groups, structural defects) TPD-MS technique was used. In such technique, the oxygen functional groups are decomposed in CO_2 and CO gases during heating, based on their thermal stability. Less stable groups such as carboxyl, lactone and anhydrides (containing $–COO^-$ groups) decompose at lower temperature by releasing CO_2 (or mixture CO_2 and CO for anhydrides), while more stable groups like phenols, quinones or ethers results in CO release at much higher temperature (>500 °C). Other gases like H_2O or H_2 can be as well evolved and can give information about the carbon surface chemistry and its structure. Therefore, the CO and CO_2 desorption profiles of the hard carbon materials are shown in Fig. 6 while those for H_2O and H_2 in Fig. S6, SI.

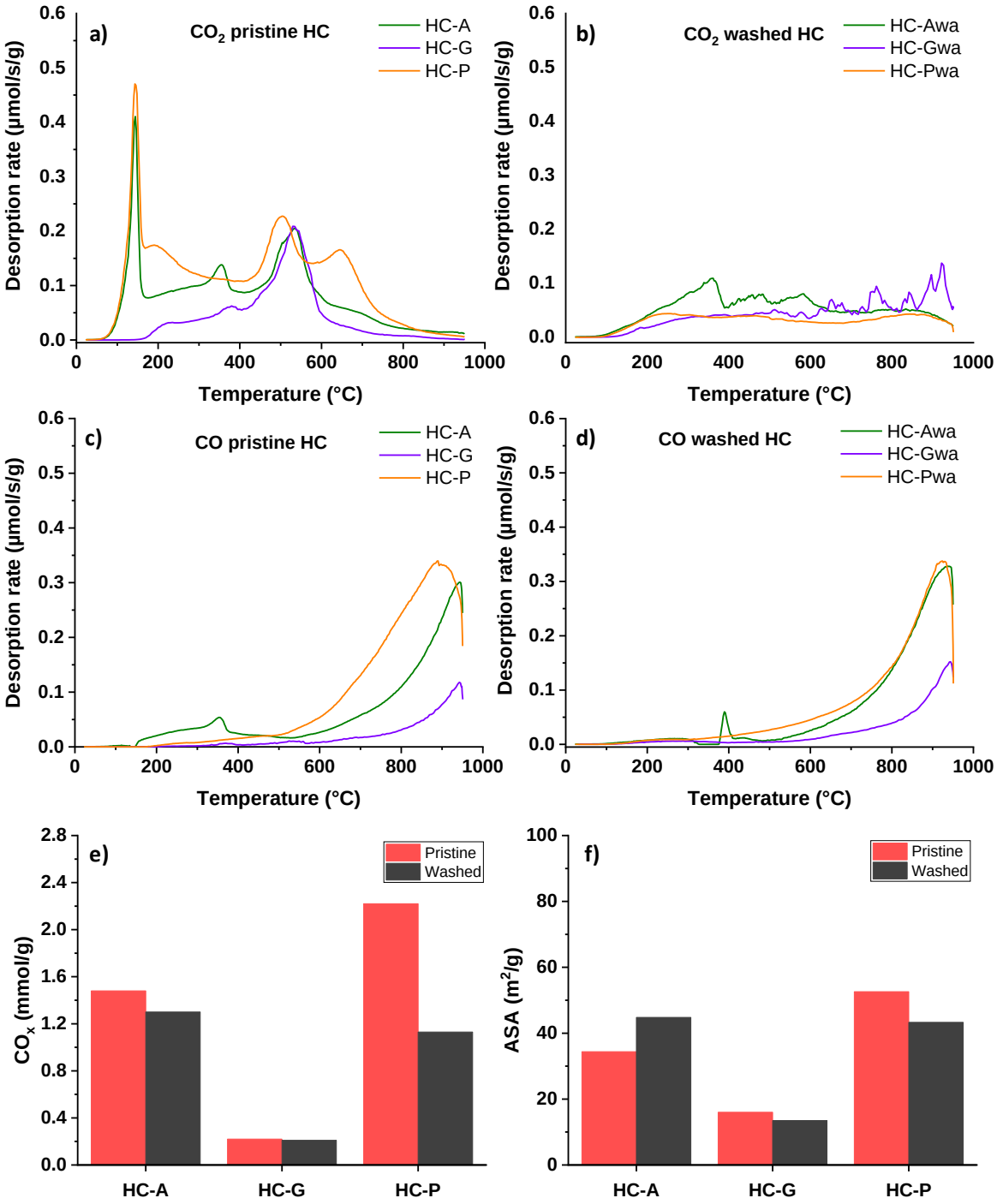

Figure 6. CO_2 and CO TPD-MS desorption profiles for pristine (a, c) and washed (b, d) hard carbons e) Desorbed quantities of oxygen-based functional groups, CO_x (CO + CO_2) and f) Active Surface Area of pristine and washed hard carbon materials after the TT.

A significant release of CO_2 occurs at low temperature (~ 150°C) for HC-A and HC-P (Figure 6a), due to carboxyl groups decomposition [49]. This is accompanied by an intense peak of concomitant H_2O desorption (Figure S6, SI). At a first glance, this can be related to physisorbed water considering the large amount of ultramicropores in these materials (Table

2). Moreover, the carbonates found in the structure could be hydrated and their decomposition lead to water release, as well. For HC-G, the low temperature intense H_2O peak is not observed which can be understood taking into account the very low porosity. Instead, a broad water peak is released at higher temperature (200-300°C) and its origin could be the hydrophilic surface given the large oxygen content related to impurities.

A significant release of CO_2 occurs at low temperature (~150 °C) for HC-A and HC-P (Fig. 6a), due to carboxyl groups decomposition [49]. This is accompanied by an intense peak of concomitant H_2O desorption (Fig. S6, SI). At a first glance, this can be related to physisorbed water considering the large amount of ultramicropores in these materials (Table 2). Moreover, the carbonates found in the structure could be hydrated and their decomposition might lead to water release, as well. For HC-G, the low temperature intense H_2O peak is not observed which can be understood taking into account the very low porosity. Instead, a broad water peak is released at higher temperature (200–300 °C) and its origin could be the hydrophilic surface given the large oxygen content related to impurities.

Moreover, in the temperature range 400–550 °C, an intense CO_2 peak is present for all materials (Fig. 6a) which is quite surprising for a hard carbon, taking into consideration that CO_2 coming from oxygen-based functional groups decomposes at lower temperatures. Such behavior, however, has been reported recently for lignin-derived carbons [28] and may be caused by the decomposition of metal carbonate which has a higher thermal stability. For HC-P, a supplementary CO_2 peak is seen even at higher temperature (650 °C), suggesting even more stable carbonate decomposition. Moreover, when the washed materials were analyzed (Fig. 6b), these CO_2 peaks disappears, thus confirming the hypothesis of the origin of these peaks.

Regarding, the stable oxygen groups, the CO desorption profiles (Fig. 6c, d) show just one intense peak reaching the maximum intensity at temperatures higher than 900 °C. Usually, the CO peak is seen in the temperature range 500–800 °C as a result of the decomposition of functional groups such as phenol, ether, carbonyl or quinones. Of these, quinones are the most stable and the presence of an important amount could cause the release of CO at higher temperatures. Compared to other hard carbons reported in the literature [35,50,51] showing a large pallet of stable oxygen-based groups, the desorption profiles herein are very different. Worth to mention, that previous works did not concern complex biomass but rather bio-polymer derived HCs. Regarding the amount of desorbed functional groups, it can be seen in Fig. 6e that

washing leads to a decrease in the amount of CO_x groups as follows: from 1.5 for HC-A to 1.3 mmol g^{-1} for HC-Awa and from 2.2 for HC-P to 1.1 mmol g^{-1} for HC-Pwa. In the case of HC-G, no significant change is noted after washing.

When active surface area was determined for pristine and washed HCs, a slightly different trend was observed: an increase after washing from 34 to 45 m^2 g^{-1} for HC-Awa while for grape waste and potato peel derived carbons a decrease was observed after washing as follows, from 16 to 13 m^2 g^{-1} in the case of HC-Gwa and from 53 to 43 m^2 g^{-1} for HC-Pwa (Fig. 6f). Given the high temperature at which the thermal treatment was performed and the fact that the materials were not functionalized/activated, such high values (except grape waste derived HC) are particularly high compared to previous works on HC. It should be mentioned however, that this is the first report, to our knowledge, where the surface chemistry and active sites were determined by TPD-MS technique for biomass derived hard carbons. For instance, for some bio-polymers derived hard carbons, the reported values of ASA can be given for comparison purposes. Lignin has values between 9 and 13 m^2 g^{-1} [28], cellulose ~16 m^2 g^{-1}, cotton 9.4 m^2 g^{-1} [50] and polyacrylonitrile, PAN ~1.2 m^2 g^{-1} [52]. Several reasons may be proposed to explain these high values for the HCs herein prepared. For instance, the ASA increase after washing, observed for HC-Awa can be explained to some extent by the increase of SSA after washing since the structural defects are directly dependent of SSA. An almost linear dependence between ASA and SSA was reported in the literature, when different cellulose derived HCs were studied [51]. It is important to remind that ASA represents the surface of edge planes/defects of carbon, while the total surface area of carbon basal planes it is given by the BET SSA. Therefore, sometimes is more pertinent to determine the ratio between the ASA and the BET SSA to have an estimation of the edge defects reported to the basal plans. We can see (Table 2) that these ratios follow the same trend for all materials and decreases after washing as follows: from 4.9 to 1.1 for asparagus HC, from 2.6 to 1.6 for grape waste HC and from 4.5 to 1.2 for potato HC.

However, the presence of impurities must also be taken into account. To recall, the determination of ASA implies the HC surface to be initially cleaned by a heat treatment at 950 °C, under vacuum. This step leads firstly to the thermal decomposition of metal carbonate with formation of metal oxide and CO_2 and further to the metal oxide reduction to its metal form via carboreduction reactions (2). Further the carbon is exposed to O_2 at 300 °C for 10 h, thus, the metal impurities present in the structure may react with O_2 forming metal oxides,

according to the Eq. 3. During the new TPD-MS measurement done after surface cleaning and oxygen chemisorption to determine ASA, these oxides react with C at high temperatures and lead to the release of a significant amount of CO_x (4):

$$MCO_3 \rightarrow MO + CO_2;\ MO + C \rightarrow M + CO \quad (1)$$

$$M + O_2 \rightarrow MO_x \quad (2)$$

$$MO_x + C \rightarrow M\ (g) + CO_x\ (g) \quad (3)$$

Therefore, the obtained ASA values cannot be linked just to the structural defects on HC structure but also to the metallic impurities that lead to the formation of a large amount of CO/CO_2. Thus, even if the SSA slightly increases after washing in the cases of HC-Gwa and HC-Pwa, impurities removal and implicitly metal oxides removal leads to formation of less functional groups. As result, the overall measured ASA value is lower. On the other hand, the ASA increase found for HC-Awa can be related to a more significant SSA increase after washing and to the larger percentage of impurities found in the structure (based on EDX results) as compared to the other samples (8.9 wt% for HC-Awa *vs.* 5.6 wt% for HC-Gwa and 3.9 wt% for HC-Pwa). Moreover, considering that the difference between pristine and washed HCs ASA values is not significant (see Table 2) this explanation may be plausible.

An important conclusion that emerges from materials surface chemistry analysis is that particular care must be paid to distinguish between the oxygenated groups coming from functional groups and impurities. In addition, the inability to quantify the active surface area of carbon itself without impurities contribution (due to the heterogeneous structure) must be underlined too. Unfortunately, these aspects are not taken into account in the literature when hard carbons are developed from a wide range of biowaste precursors and explored as anodes for NIBs.

We can conclude at this point that the presence of impurities has an important influence on the materials characteristics, especially on the textural properties (higher SSA as a result of the free spaces left by the impurities) and the surface chemistry, *i.e.*, increased amount of functional groups, structural defects. Moreover, the complexity of the surface chemistry caused by the presence of impurities can be easily modified even by exposure to air under ambient conditions. Regarding materials structure, it was found that the presence of impurities can affect the d-spacing, lower values being obtained after washing due to their localization between the graphene layers and in some cases their strong interaction with carbon during the thermal treatment led to higher graphitization degrees.

3.5. Hard carbon electrochemical performance

First, HC materials conductivity was determined with the help of EIS (Electrochemical Impedance Spectroscopy). The link between the HC inorganic impurities/heteroatoms and the electronic conductivity is not well known.

The results shown in Fig. 7, reveals an improvement in the materials electronic conductivity after the washing step. This could be related to the decrease of oxygen and impurities content. More importantly, when the materials conductivity is represented in ascending order, a clear trend can be observed (Fig. 7b); the electronic conductivity increases with the carbon content and with the decrease of impurities/oxygen content.

For HC-G and HC-Pwa, the atypical conductivity behavior seems to be linked not only to C and O content, but also to their structure which present graphitized domains (see HR-TEM, Fig. 4) and contributes positively to the electronic conductivity enhancement. Thus, the graphitization degree of the materials is also determinant in the control of materials conductivity.

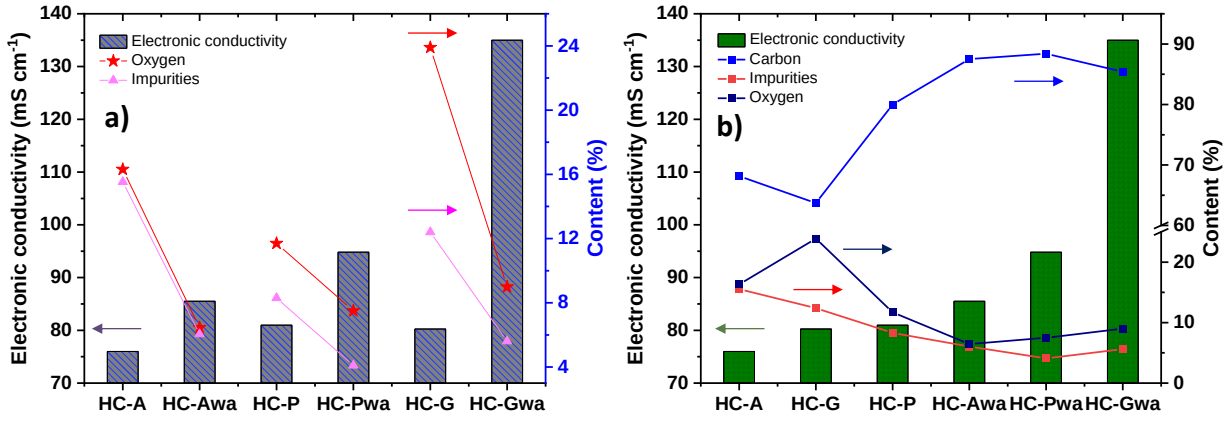

Figure 7. a) Electronic conductivity of the pristine and washed hard carbon materials versus oxygen and impurities content. b) Ascending evolution of the electronic conductivity and the correlations with the carbon, oxygen and impurities contents.

Further, the presence/absence of impurities influence on the Na^+ storage mechanism and the delivered performance was evaluated. The electrochemical behavior was studied by both CV and GCPL techniques. In Fig. 8, the CV results of the materials analyzed with a scan rate of 0.2 mV s^{-1} in the voltage window 0.01–2 V under ambient conditions are shown.

All HC materials (pristine and washed) exhibit in the first cycle an irreversible broad shoulder at approx. 0.4 V which can be attributed to the formation of solid electrolyte interphase (SEI) layer due to electrolyte decomposition upon contact with Na metal [53].

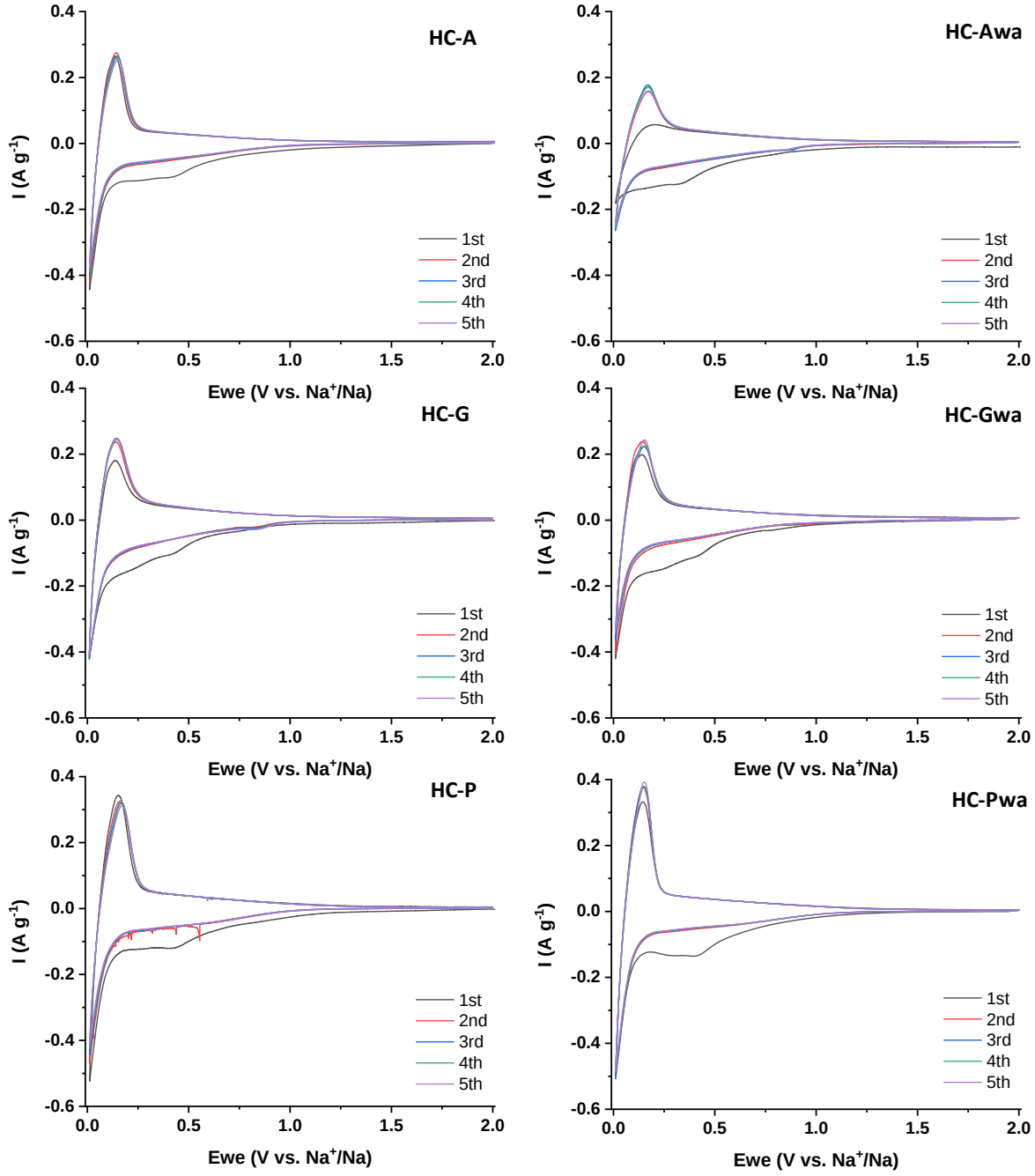

Figure 8. Cyclic voltammograms of pristine (left) and washed biowaste (right) derived HCs from 2-electrodes tests.

The origin of this peak is confirmed by its disappearance in the following cycles, being known that the formation of SEI takes place only in the first cycle. HC-P presents some small

and sharp cathodic peaks during the 2nd cycle, which can be rather related to experimental issues, coming from the electrode or from the cell itself. Besides that, there is no evidence of redox reactions between the metal impurities and the electrolyte/sodium ions. Near 0 V, two redox peaks can be seen for all samples, attributed to the reversible insertion-extraction of sodium ions into the HC graphene layers [54], similarly to Li ions insertion/extraction within graphite, in lithium ion batteries [17,21,55].

Galvanostatic and potentiostatic measurements were coupled to determine the quantitative performance of the materials and the obtained profiles are presented in Fig. 9. At the end of each galvanostatic discharge/charge cycle a potentiostatic step of 1 h was added (the cell is maintained at constant voltage) to fully complete the sodium insertion-extraction in/from the hard carbon host.

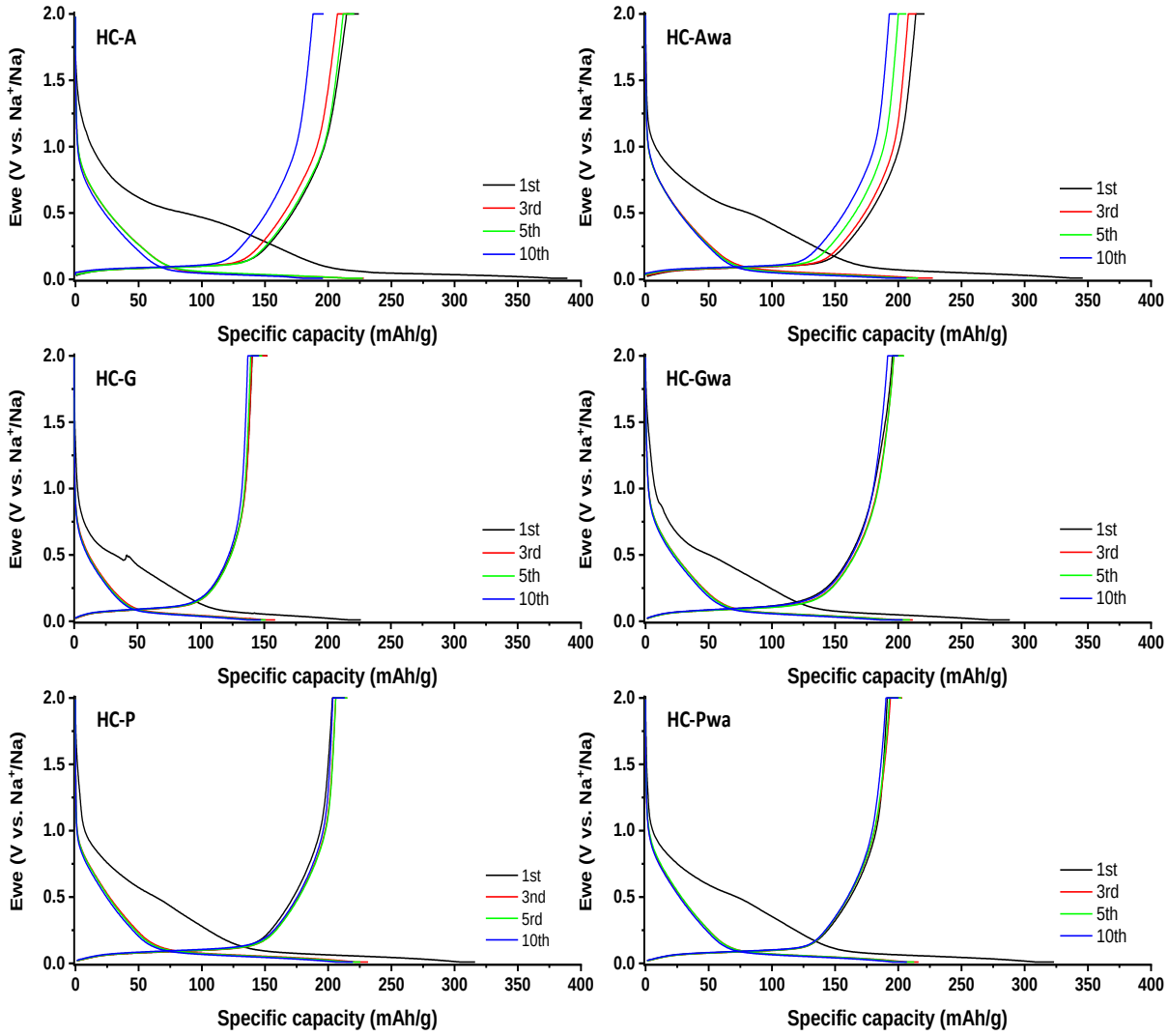

Figure 9. GCPL profiles of 1st, 3rd, 5th and 10th cycles. Comparison between pristine (left) and washed (right) HCs cycled at C/10 rate.

An initial discharge capacity as high as 390 mAh g^{-1} could be delivered by HC-A, 227 mAh g^{-1} for HC-G and 317 mAh g^{-1} for HC-P. However, the 1st charge capacity reaches much lower values, respectively 180 mAh g^{-1} for HC-A, 153 mAh g^{-1} for HC-G and 214 mAh g^{-1} for HC-P. The significant difference is caused by a high initial irreversible capacity, especially in the case of HC-A, leading to a low iCE of only 46%, while for HC-G and HC-P a higher iCE was observed, 67%. It has been reported before that the texture and the surface chemistry of the materials may induce irreversible reactions and SEI layer formation in the first cycle [51,56]. Therefore, the large initial irreversible capacity found for the HCs could be rather related to the surface functional groups and/or heteroatoms (that may react with the electrolyte and cause its decomposition) since both N_2 and CO_2 SSA have small values. This explanation is plausible and is confirmed by HC-Awa for which iCE increases after washing from 46% to 64% while the capacity improves from 180 mAh g^{-1} to ~220 mAh g^{-1}. However, the increase of SSA with impurities removal could limit the achievement of higher performance since facilitates irreversible reactions.

In the case of HC derived from pristine grape waste, a smaller reversible capacity was obtained (153 mAh g^{-1}) and might be associated to the lower d-spacing and amount of defects. Considering the most recent reports on Na storage mechanisms [50,51,57,58], the slope capacity is assign to adsorption of Na^+ in the porosity and on the active sites while the low voltage plateau is related to Na^+ intercalation between the graphene plans. It is important to mention, however, that this mechanism is still under debate [52,59,60], the reason behind being the complex HC structure leading to ambiguous interpretations. Therefore, after washing, as the HC-Gwa material shows slightly higher porosity, the capacity gained on the slope region is more important and a reversible capacity of 204 mAh g^{-1} is obtained, in agreement with the storage mechanism before mentioned. It is also important to mention that washing induces an increase in the carbon content which is favorable for Na storage and thus might explain the observed improvement. The iCE slightly increases as well, and reaches 71% (*vs.* 67%). For potato peel derived HC, the values are rather similar: 214 mAh g^{-1} reversible capacity and 67% iCE for HC-P while for HC-Pwa a reversible capacity of 202 mAh g^{-1} and 62% iCE was obtained (see Fig. 10a, b). Given that the lower performance is associated to a lower capacity obtained on the plateau region, it is possible that the structural changes that occurred after washing (lower d-spacing and disorder degree) were the cause. Additionally, even if both ASA and functional groups are lower after washing, they still present high values. This may favor

the electrolyte decomposition and SEI formation, limiting thus the material to deliver higher performance.

Given the complex and heterogeneous nature of these anode materials, a question mark may arise regarding the reproducibility of the results. To check this, a second cell was assembled for each material and analyzed in the same conditions. The GCPL results are presented in Fig. S7, SI. Concerning the reversible capacity, it can be seen that generally the two identical cells deliver similar performance (91–98% reproducibility) with two exceptions, *i.e.*, HC-G (82%) and HC-P (86%). However, when it comes to the initial discharge, important differences could be observed, and we believe that it might be related to materials composition which is not homogeneous and thus, the electrodes obtained are heterogeneous. As result, the irreversible reactions that take place in the first cycle are different. In consequence, the initial Coulombic efficiency among the two cells present only small variations, exept for HC-A and HC-Pwa.

A good stability was seen for both grape waste and potato peel derived HCs (pristine and washed materials) in the first 10 cycles while asparagus peel derived HC (washed or not) shows a small capacity fading (see Table S5, SI). Further, HC-A and HC-Awa were tested for several more cycles at C/10 rate and the results are shown in Fig. 10c, d. Besides some local fluctuations, HC-A capacity is very stable in the first 50 cycles while the CE reaches 100% after the first 5 cycles. Regarding the washed sample, HC-Awa, one can see how the capacity gradually decreases during the first apx. 35 cycles after which it becomes relatively constant. The CE shows gradually increase until 100% (around cycle 30), and remains rather constant in the subsequent cycles.

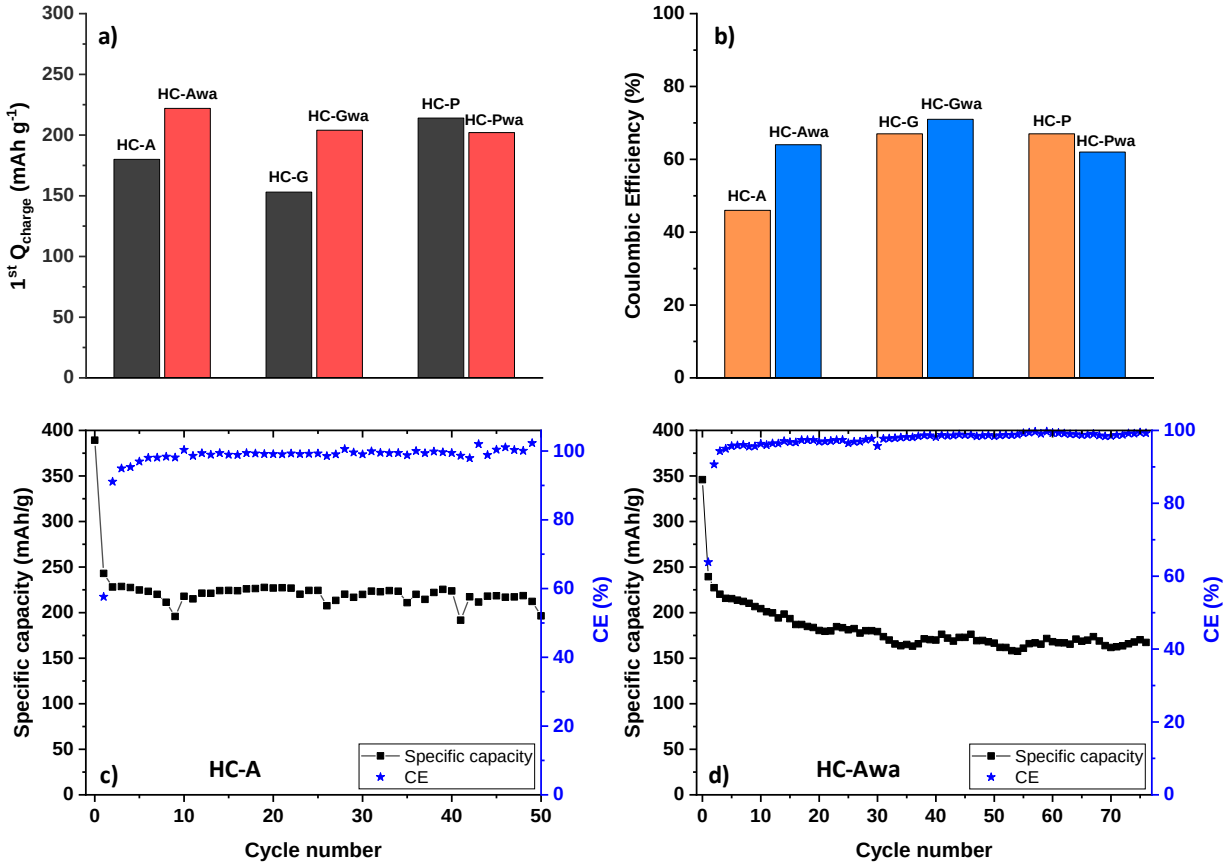

Figure 10. a) First cycle charge capacity and b) initial Coulombic efficiency of the hard carbon materials. Long term cycling along with CE of asparagus derived HC: c) pristine and d) washed.

Although the materials features are highly modified by the presence of impurities, the electrochemical tests performed on pristine and washed HCs showed rather similar performance. This outcome could be explained by some concomitant modification of carbon properties after washing. The removal of impurities which could trigger positive effects on the electrochemical performance are outbalanced by the increase of SSA and decrease of interlayer space. Therefore, the possible benefit coming from the absence of the impurities is hindered by the microstructural changes. This is the reason why washing done before heat-treatment was explored to evaluate its efficiency in removing the impurities and to asses the structural and textural changes along with the electrochemical behavior.

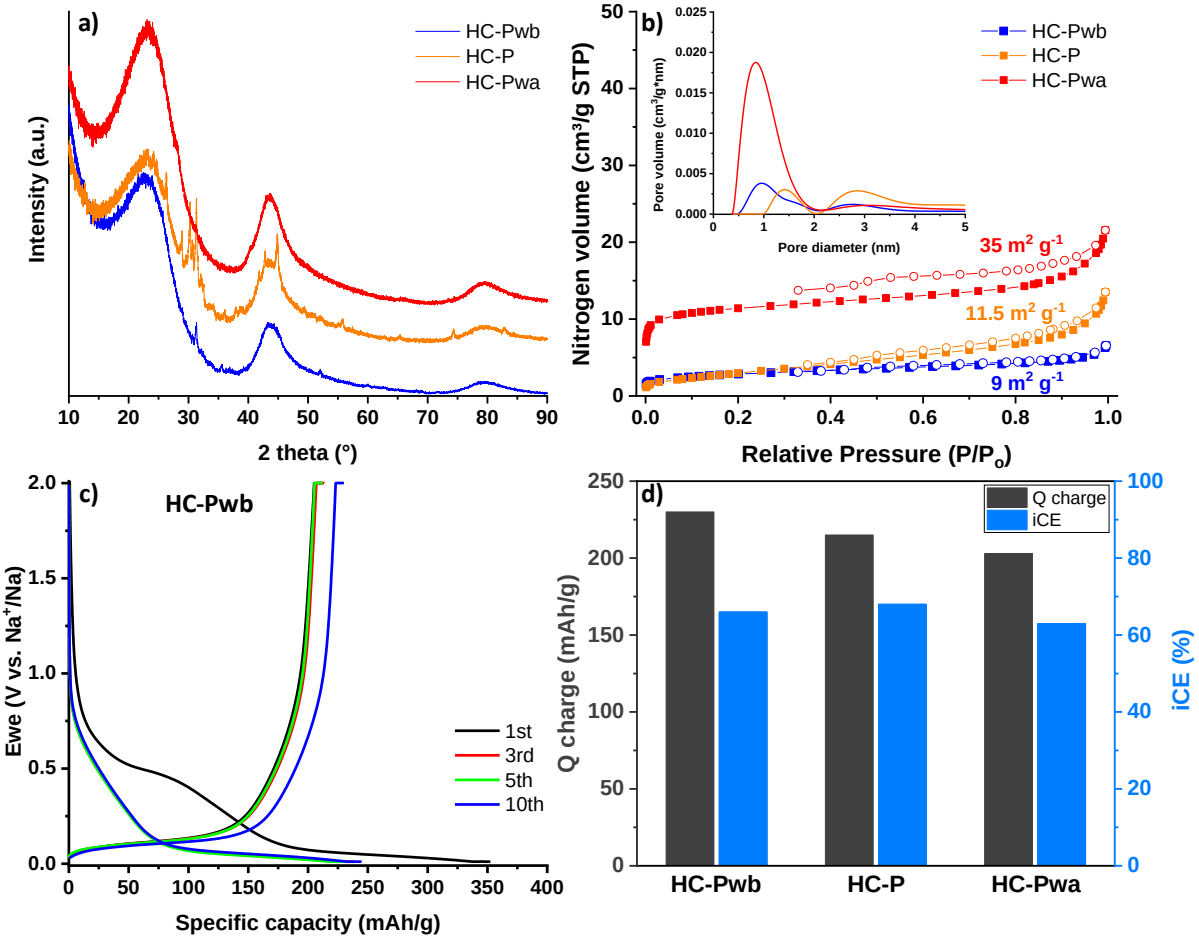

Figure 11. a) XRD data and b) N_2 adsorption-desorption isotherms and pore size distribution (inset) of HC-Pwb, HC-P and HC-Pwa potato peel derived hard carbons. c) GCPL profiles for HC-Pwb and d) Reversible capacity and iCE of HC-Pwb, HC-P and HC-Pwa materials.

The situation when washing is done before the TT was considered (thus the precursors are washed and not the hard carbon). To avoid any modification on the biomass structure due to HCl solution, washing was performed with hot distilled water only (60 °C). Potato derived sample was selected since the washing done after the heat-treatment resulted in the complete impurities removal while HC-Gwa and HC-Awa still have traces of impurities. The materials were denoted in this case HC-Xwb (wb-washed before TT), where "X" represents the precursor used. Fig. 11 shows materials characteristics obtained for potato waste derived HC, taking into account the three cases studied: pristine (HC-P), washing after TT (HC-Pwa) and washing before the TT (HC-Pwb).

The XRD diffractograms of potato derived carbons (Fig. 11a, blue trace) shows that washing with distilled water was very efficient and removed the vast majority of impurities (only a small peak could still be seen at a 2-theta value of 31°), while the d-spacing has similar value to HC-P, 3.93 Å. EDX data confirm these results as the weight percentage of inorganic impurities is about 1.5 wt% for HC-Pwb (washed before TT), significantly lower than both pristine (8.5 wt%) and washed after TT hard carbons (~ 4 wt%), Table S6, SI. These results highlight as well the efficiency of the washing before the pyrolysis step.

The amorphous carbon structure is maintained when washing is done before the heat-treatment (HC-Pwb), as confirmed by both Raman and HR-TEM analyses. Raman spectra of the three materials are very similar (Fig. S8, SI) and a high disorder degree was found. However, both washed materials (HC-Pwb and HC-Pwa) present lower I_D/I_G values (1.9 and 2.0, respectively) compared to the pristine one (2.5 for HC-P).

HR-TEM reveals the turbostratic structure of HC-Pwb (Fig. S9, SI) with few graphene layers stacked and random orientation, similar to HC-P and HC-Pwa structures. Differently from the HC-Pwa, where the removal of the impurities after pyrolysis led to the creation of mesopores, the HC-Pwb washed before pyrolysis does not show any mesopores. The textural properties analyzed by N_2 adsorption-desorption technique (Fig. 11b) shows the same type II isotherm for HC-Pwb, typical for non-porous materials. No hysteresis is observed suggesting the absence of mesopores, in agreement with the HR-TEM results. The SSA is similar to the pristine hard carbon, *i.e.*, 9 $m^2 g^{-1}$ for HC-Pwb and 11.5 $m^2 g^{-1}$ for HC-P, differently from HC-Pwa for which SSA increased to 35 $m^2 g^{-1}$. Similar trend is observed for the pore size distribution (inset Fig. 11b). The higher specific surface area and the presence of mesopores for the material washed after pyrolysis (HC-Pwa), suggest a preferential location of impurities in both micro - and meso-pores.

Further, HC-Pwb surface chemistry was evaluated by TPD-MS and compared with the pristine and washed after TT hard carbons (Fig. S10, SI). Overall, washing done before the annealing treatment (HC-Pwb) reduces significantly both the oxygenated functional groups (*i.e.*, 0.72 mmol g^{-1} for HC-Pwb *vs.* 2.22 mmol g^{-1} for HC-P and 1.13 mmol g^{-1} for HC-Pwa) and the active sites of the material (*i.e.*, 11.5 $m^2 g^{-1}$ for HC-Pwb *vs.* 52.6 $m^2 g^{-1}$ for HC-P and 43.3 $m^2 g^{-1}$ for HC-Pwa), when compared with the pristine and washed after TT carbons (Table 2). The results confirm that washing done before the thermal treatment is more efficient in impurities removal leading to characteristics slightly improved when compared to HC-Pwb.

The structural features of HC-Pwb are rather similar to HC-Pwa while the specific surface area, the functional groups and the active sites are lower for HC-Pwb. It is interesting to see further how the electrochemical properties of HC-Pwb are affected. GCPL measurements were done for HC-Pwb and the results are shown in Fig. 11c, d. The delivered capacity is just slightly higher than HC-P and HC-Pwa. HC-Pwb could reach in the 1st discharge a capacity of 350 mAh g^{-1} and a reversible capacity of 215 mAh g^{-1}, corresponding to an iCE of 66%. However, after 10 cycles the material delivers a reversible capacity of 230 mAh g^{-1}. To better visualize the electrochemical behavior of the three materials, the 1st, 3rd and 10th cycles were compared and the results are shown in Fig. S11, SI. In the first cycle HC-Pwb present a more defined shoulder at around 0.7 V due to electrolyte decomposition and SEI layer formation. Moreover, while switching from discharge to charge, a small overpotential (0.03 V) can be observed for HC-Pwb, related most likely to an unstable SEI layer, thus limiting the delivered capacity. This behavior is observed in the 3rd cycle, as well, but in the 10th cycle, the overpotential is no longer occurring. As result, once a stable SEI layer build up (10th cycle), the exhibited capacity is higher than both HC-P and HC-Pwa. The normalized discharge-charge curves (Fig. S11, SI) confirm, as well, that besides the first cycle where the sloping region is different, the three materials present very similar electrochemical behavior.

These tests performed on the material washed before TT, although preliminary, tend to show that better performance could be achieved than both the pristine and the HC washed after TT. This can be explained by the combined low surface area with less surface functional groups and structural defects and thus more significant inorganic impurities removal. Moreover, since this washing is done only in the presence of distilled water it is preferred over the one done on the HC with HCl solution. The capacity delivered by these materials can be still improved, particularly by increasing the carbon content in the materials (which is still low, *i.e.*, 83–87.5 wt%) in the detriment of oxygen, by favorably increasing the pyrolysis temperature as shown elsewhere [45,61,62].

To test this hypothesis two water washed biomasses (asparagus and potato) were thermally treated at 1400 °C and the resulting HCs were electrochemically tested. The GCPL results are presented in Fig. S12, SI. The delivered reversible capacity improved for both materials and reached 280 mAh g^{-1}. The enhancement of the pyrolysis temperature from 1300 °C to 1400 °C increased thus the capacity with 50 mAh g^{-1} for HC-Pwb and 70 mAh g^{-1} for HC-Pwa.

Moreover, the electrochemical impedance spectroscopy was performed on the two materials (HC-Awb 1400 and HC-Pwb 1400) before cycling and after 5 discharge-charge cycles. For both cases, the Nyquist plots (Fig. S13, SI) are composed of an extended tail in the low-frequency region and related to diffusion phenomenon, a semicircle in the middle-frequency region caused by charge transfer reactions at the electrode surface and finally, a small curve that intersects the x-axis at high frequency, assigned to the cell inductance and ohmic resistance.

For HC-Awb 1400 material (Fig. S13a, SI), a big semicircle could be observed before cycling the cell, which suggest high resistance at the electrode-electrolyte interface. After the 5th charge/discharge cycle, the semicircle become less pronounced, the resistance decreases and the charge transfer improves due to the formation of a conductive SEI layer.

Worth to mention that the semicircle does not intersect the x-axis in "0", sign of electrolyte resistance, which seems to slightly increase over cycling (from 5 Ohms before cycling to 8 Ohms after the 5th cycle). Concerning Na^+ diffusion given by the low-frequency tail, one can see similar behavior between the two Nyquist plots, meaning that no significant changes occur over cycling.

For HC-Pwb 1400 (Fig. S13b, SI), a similar behavior is observed involving electrolyte resistance (semicircle does not intersect in "0") and high resistance at the electrode surface as suggested by the semicircle present in the middle-frequency region (1.3 Hz). Further, within cycling, the charge transfer reaction at the electrode surface improves, being indicated by the lower resistance revealed by the semicircle reaching higher frequencies (14 Hz). For this material, the main difference is given by the low-frequency tail, meaning that in this case Na^+ diffusion changes significantly over cycling.

Therefore, we believe that these results confirm that it is further possible to optimize the biomass derived hard carbons properties to obtain better electrochemical performance.

4. CONCLUSIONS

The influence of naturally occurring structural impurities in biomass waste, on hard carbon preparation and on both physico-chemical and electrochemical properties in Na-ion batteries, was studied, herein. Such aspects which are of prime importance for large scale application of these available, cheap and abundant resources are rarely discussed in the literature.

A first approach consisted in material washing after pyrolysis, which revealed that the high amount of inorganic alkaline impurities could be largely removed. A decrease of the $d_{(002)}$ interlayer distance was observed, that could be correlated to the removal of the inserted ions between the graphene planes. For grape waste derived HC, the local graphitization induced by impurities during the thermal annealing, prevent impurities trapped inside the graphite interlayer space to move outside the material during washing. An important porosity increase, due to the formation of *-ultramicro*, *−micro* and *–meso* pores after washing was observed as well, except once again for grape derived carbon. Regarding the surface chemistry, the presence of impurities played a very important role due to their high reactivity when exposed to air, resulting in a large amount of oxygen bonded to inorganic impurities. Consequently, after washing the surface chemistry and the structural defects, although challenging to precisely quantify, diminished. The electronic conductivity significantly improved for all materials after the removal of impurities.

The electrochemical tests showed that the performance of pristine and washed after TT samples is rather similar. No general tendency among the materials could be established owing to the impact of several interplaying carbon properties on the performance. The reversible capacity was improved after washing for HC-Awa and HC-Gwa while for HC-Pwa remained rather constant. Although some materials have reached high capacity during the first discharge (*i.e.*, 390 mAh g^{-1} for HC-A), a significant initial irreversible capacity was observed. This could be related to the high impurities content in pristine carbons, which, even successfully removed after washing, induced a higher SSA, known as detrimental for sodium storage. The high amount of oxygen and defects explained also the observed results. Alternative approach, where the precursor was washed before the heat treatment (using water instead of HCl) was also studied and better efficiency regarding the removal of inorganic impurities was observed. The performed electrochemical tests revealed that, the reversible capacity modestly exceeded the values for pristine materials and washed materials after TT. Higher pyrolysis temperature applied to the water washed materials allowed further to improve the reversible capacity from 230 mAh g^{-1} (1300 °C) up to 280 mAh g^{-1} (1400 °C).

The assembly of results presented here offers many insights about the impact of the impurities on the hard carbon features and performance. This can serve as guideline towards green and mild approaches to be further explored for sustainable fabrication of hard carbon.

Nevertheless, extended studied are still required on a wider range of biomass-derived materials to obtain a more general overview about biomass-HC synthesis cost for competitive implementation in real devices.

Declaration of Competing Interest

The authors declare that they have no known competing financial interests or personal relationships that could have appeared to influence the work reported in this paper.

Acknowledgments

This work was performed in the frame of RS2E (French research network on electrochemical energy storage), and the laboratory of excellency for electrochemical energy storage, STORE-EX. The authors thank DGA (Direction Générale de l'Armement, N° 2016 60 0050) and Region Alsace (N° 618342) for the financial support of this work. We also thank Dr. Loic Vidal (HRTEM images) and Dr. Stephan Knopf (EDX analysis) for technical support via IS2M technical platforms. We express our recognition to M. François Rabuel and LRCS laboratory from Amiens, for the help received for the electrochemical tests.

Appendix A. Supplementary data

REFERENCES

[1] S. Zheng *et al.*, "Transition-Metal (Fe, Co, Ni) Based Metal-Organic Frameworks for Electrochemical Energy Storage," *Adv. Energy Mater.*, vol. 7, no. 18, p. 1602733, Sep. 2017, doi: 10.1002/aenm.201602733.

[2] X. Li, X. Yang, H. Xue, H. Pang, and Q. Xu, "Metal–organic frameworks as a platform for clean energy applications," *EnergyChem*, vol. 2, no. 2, p. 100027, May 2020, doi: 10.1016/j.enchem.2020.100027.

[3] J. Górka, C. Vix-Guterl, and C. Matei Ghimbeu, "Recent Progress in Design of Biomass-Derived Hard Carbons for Sodium Ion Batteries," *C*, vol. 2, no. 4, p. 24, Dec. 2016, doi: 10.3390/c2040024.

[4] S. Guo, J. Yi, Y. Sun, and H. Zhou, "Recent advances in titanium-based electrode materials for stationary sodium-ion batteries," *Energy Environ. Sci.*, vol. 9, no. 10, pp. 2978–3006, Oct. 2016, doi: 10.1039/C6EE01807F.

[5] J.-Y. Hwang, S.-T. Myung, and Y.-K. Sun, "Sodium-ion batteries: present and future," *Chem. Soc. Rev.*, vol. 46, no. 12, pp. 3529–3614, Jun. 2017, doi: 10.1039/C6CS00776G.

[6] T. Liu and X. Li, "Biomass-derived nanostructured porous carbons for sodium ion batteries: a review," *Mater. Technol.*, vol. 34, no. 4, pp. 232–245, Mar. 2019, doi: 10.1080/10667857.2018.1545392.

[7] I. El Moctar, Q. Ni, Y. Bai, F. Wu, and C. Wu, "Hard carbon anode materials for sodium-ion batteries," *Funct. Mater. Lett.*, vol. 11, no. 06, p. 1830003, Dec. 2018, doi: 10.1142/S1793604718300037.

[8] R. Li *et al.*, “Controlling the Thickness of Disordered Turbostratic Nanodomains in Hard Carbon with Enhanced Sodium Storage Performance,” *Energy Technol.*, vol. 6, no. 6, pp. 1080–1087, 2018, doi: 10.1002/ente.201700674.
[9] K. Hong *et al.*, “Biomass derived hard carbon used as a high performance anode material for sodium ion batteries,” *J. Mater. Chem. A*, vol. 2, no. 32, pp. 12733–12738, Jul. 2014, doi: 10.1039/C4TA02068E.
[10] K. Wang *et al.*, “Low-Cost and High-Performance Hard Carbon Anode Materials for Sodium-Ion Batteries,” *ACS Omega*, vol. 2, no. 4, pp. 1687–1695, Apr. 2017, doi: 10.1021/acsomega.7b00259.
[11] J. Xiang, W. Lv, C. Mu, J. Zhao, and B. Wang, “Activated hard carbon from orange peel for lithium/sodium ion battery anode with long cycle life,” *J. Alloys Compd.*, vol. 701, pp. 870–874, Apr. 2017, doi: 10.1016/j.jallcom.2017.01.206.
[12] E. M. Lotfabad *et al.*, “High-Density Sodium and Lithium Ion Battery Anodes from Banana Peels,” *ACS Nano*, vol. 8, no. 7, pp. 7115–7129, Jul. 2014, doi: 10.1021/nn502045y.
[13] S.-D. Xu *et al.*, “Curly hard carbon derived from pistachio shells as high-performance anode materials for sodium-ion batteries,” *J. Mater. Sci.*, vol. 53, no. 17, pp. 12334–12351, Sep. 2018, doi: 10.1007/s10853-018-2472-4.
[14] W. Lv *et al.*, “Peanut shell derived hard carbon as ultralong cycling anodes for lithium and sodium batteries,” *Electrochimica Acta*, vol. 176, pp. 533–541, Sep. 2015, doi: 10.1016/j.electacta.2015.07.059.
[15] M. Dahbi *et al.*, “Synthesis of Hard Carbons from Argan Shell for Na-Ion Batteries,” *J. Mater. Chem. A*, vol. 5, no. 20, pp. 9917–9928, May 2017, doi: 10.1039/C7TA01394A.
[16] K. Kim *et al.*, “Tailored Carbon Anodes Derived from Biomass for Sodium-Ion Storage,” *ACS Sustain. Chem. Eng.*, vol. 5, no. 10, pp. 8720–8728, Oct. 2017, doi: 10.1021/acssuschemeng.7b01497.
[17] H. Wang, W. Yu, J. Shi, N. Mao, S. Chen, and W. Liu, “Biomass derived hierarchical porous carbons as high-performance anodes for sodium-ion batteries,” *Electrochimica Acta*, vol. 188, pp. 103–110, Jan. 2016, doi: 10.1016/j.electacta.2015.12.002.
[18] C. del M. Saavedra Rios, V. Simone, L. Simonin, S. Martinet, and C. Dupont, “Biochars from various biomass types as precursors for hard carbon anodes in sodium-ion batteries,” *Biomass Bioenergy*, vol. 117, pp. 32–37, Oct. 2018, doi: 10.1016/j.biombioe.2018.07.001.
[19] Q. Wang, X. Zhu, Y. Liu, Y. Fang, X. Zhou, and J. Bao, “Rice husk-derived hard carbons as high-performance anode materials for sodium-ion batteries,” *Carbon*, vol. 127, pp. 658–666, Feb. 2018, doi: 10.1016/j.carbon.2017.11.054.
[20] T. Zhang *et al.*, “Pinecone biomass-derived hard carbon anodes for high-performance sodium-ion batteries,” *RSC Adv.*, vol. 7, no. 66, pp. 41504–41511, Aug. 2017, doi: 10.1039/C7RA07231G.
[21] J. Ding *et al.*, “Carbon Nanosheet Frameworks Derived from Peat Moss as High Performance Sodium Ion Battery Anodes,” *ACS Nano*, vol. 7, no. 12, pp. 11004–11015, Dec. 2013, doi: 10.1021/nn404640c.
[22] X. Meng, P. E. Savage, and D. Deng, “Trash to Treasure: From Harmful Algal Blooms to High-Performance Electrodes for Sodium-Ion Batteries,” *Environ. Sci. Technol.*, vol. 49, no. 20, pp. 12543–12550, Oct. 2015, doi: 10.1021/acs.est.5b03882.
[23] H. Yamamoto *et al.*, “Synthesizing higher-capacity hard-carbons from cellulose for Na- and K-ion batteries,” *J. Mater. Chem. A*, vol. 6, no. 35, pp. 16844–16848, Sep. 2018, doi: 10.1039/C8TA05203D.
[24] S. Nam, B. D. Condon, Y. Liu, and Q. He, “Natural resistance of raw cotton fiber to heat evidenced by the suppressed depolymerization of cellulose,” *Polym. Degrad. Stab.*, vol. 138, pp. 133–141, Apr. 2017, doi: 10.1016/j.polymdegradstab.2017.03.005.
[25] H. Zhu *et al.*, “Low temperature carbonization of cellulose nanocrystals for high performance carbon anode of sodium-ion batteries,” *Nano Energy*, vol. 33, pp. 37–44, Mar. 2017, doi: 10.1016/j.nanoen.2017.01.021.
[26] Y. Li, Y.-S. Hu, H. Li, L. Chen, and X. Huang, “A superior low-cost amorphous carbon anode made from pitch and lignin for sodium-ion batteries,” *J. Mater. Chem. A*, vol. 4, no. 1, pp. 96–104, Dec. 2015, doi: 10.1039/C5TA08601A.

[27] C. Marino, J. Cabanero, M. Povia, and C. Villevieille, “Biowaste Lignin-Based Carbonaceous Materials as Anodes for Na-Ion Batteries,” *J. Electrochem. Soc.*, vol. 165, no. 7, pp. A1400–A1408, Jan. 2018, doi: 10.1149/2.0681807jes.
[28] C. Matei Ghimbeu, B. Zhang, A. Martinez de Yuso, B. Rety, and J.-M. Tarascon, “Valorizing low cost and renewable lignin as hard carbon for Na-ion batteries: Impact of lignin grade,” *Carbon*, Jul. 2019, doi: 10.1016/j.carbon.2019.07.026.
[29] C. Bommier, W. Luo, W.-Y. Gao, A. Greaney, S. Ma, and X. Ji, “Predicting capacity of hard carbon anodes in sodium-ion batteries using porosity measurements,” *Carbon*, vol. 76, pp. 165–174, Sep. 2014, doi: 10.1016/j.carbon.2014.04.064.
[30] M. Wang, Z. Yuan, S. Cheng, M. Leitch, and C. C. Xu, “Synthesis of novolac-type phenolic resins using glucose as the substitute for formaldehyde,” *J. Appl. Polym. Sci.*, vol. 118, no. 2, pp. 1191–1197, Oct. 2010, doi: 10.1002/app.32240.
[31] R. Väli, A. Jänes, T. Thomberg, and E. Lust, “D-Glucose Derived Nanospheric Hard Carbon Electrodes for Room-Temperature Sodium-Ion Batteries,” *J. Electrochem. Soc.*, vol. 163, no. 8, pp. A1619–A1626, Jan. 2016, doi: 10.1149/2.0771608jes.
[32] W. Dong, S. Yang, D. Shen, X. Wang, S. Li, and W. Sun, “Performance of pitch and glucose pyrocarbons for reversible sodium storage,” *Carbon*, vol. 124, p. 726, Nov. 2017, doi: 10.1016/j.carbon.2017.06.063.
[33] L. Wu, D. Buchholz, C. Vaalma, G. A. Giffin, and S. Passerini, “A review of hard carbon anode materials for sodium-ion batteries,” *ChemElectroChem*, vol. 3, no. 2, pp. 292–298, Feb. 2016, doi: 10.1002/celc.201500437.
[34] T. Yang *et al.*, “A Sustainable Route from Biomass Byproduct Okara to High Content Nitrogen-Doped Carbon Sheets for Efficient Sodium Ion Batteries,” *Adv. Mater. Deerfield Beach Fla*, vol. 28, no. 3, pp. 539–545, Jan. 2016, doi: 10.1002/adma.201503221.
[35] J. M. Conder, C. Vaulot, C. Marino, C. Villevieille, and C. M. Ghimbeu, “Chitin and chitosan – structurally-related precursors of dissimilar hard carbons for Na-ion battery,” *ACS Appl. Energy Mater.*, Jun. 2019, doi: 10.1021/acsaem.9b00545.
[36] X. Dou *et al.*, “Impact of the Acid Treatment on Lignocellulosic Biomass Hard Carbon for Sodium-Ion Battery Anodes,” *ChemSusChem*, vol. 11, no. 18, pp. 3276–3285, 2018, doi: 10.1002/cssc.201801148.
[37] C. del M. Saavedra Rios, L. Simonin, A. de Geyer, C. Matei Ghimbeu, and C. Dupont, “Unraveling the Properties of Biomass-Derived Hard Carbons upon Thermal Treatment for a Practical Application in Na-Ion Batteries,” *Energies*, vol. 13, no. 14, p. 3513, Jan. 2020, doi: 10.3390/en13143513.
[38] G. Moussa, C. Matei Ghimbeu, P.-L. Taberna, P. Simon, and C. Vix-Guterl, “Relationship between the carbon nano-onions (CNOs) surface chemistry/defects and their capacitance in aqueous and organic electrolytes,” *Carbon*, vol. 105, pp. 628–637, Aug. 2016, doi: 10.1016/j.carbon.2016.05.010.
[39] C. Nita, B. Zhang, J. Dentzer, and C. Matei Ghimbeu, “Hard carbon derived from coconut shells, walnut shells, and corn silk biomass waste exhibiting high capacity for Na-ion batteries,” *J. Energy Chem.*, Sep. 2020, doi: 10.1016/j.jechem.2020.08.065.
[40] X. Liu *et al.*, “Thermal degradation and stability of starch under different processing conditions,” *Starch - Stärke*, vol. 65, no. 1–2, pp. 48–60, 2013, doi: 10.1002/star.201200198.
[41] F. M. Yedro, J. García-Serna, D. A. Cantero, F. Sobrón, and M. J. Cocero, “Hydrothermal hydrolysis of grape seeds to produce bio-oil,” *RSC Adv.*, vol. 4, no. 57, pp. 30332–30339, 2014, doi: 10.1039/C4RA00429A.
[42] E. Irisarri *et al.*, “Optimization of Large Scale Produced Hard Carbon Performance in Na-Ion Batteries: Effect of Precursor, Temperature and Processing Conditions,” *J. Electrochem. Soc.*, vol. 165, no. 16, pp. A4058–A4066, Jan. 2018, doi: 10.1149/2.1171816jes.
[43] N. Kourkoumelis, “PowDLL, a reusable .NET component for interconverting powder diffraction data: Recent developments,” *ICDD Annual Spring Meetings*. 28 (2013) 137-48 (accessed Mar. 29, 2020).
[44] T. Roisnel and J. Rodríguez-Carvajal, “WinPLOTR: A Windows tool for powder diffraction patterns analysis,” *Materials Science Forum, Proceedings of the Seventh European Powder*

Diffraction Conference (EPDIC 7). Ed. R. Delhez and E. J. Mittenmeijer, 2000, p. 118. (accessed Mar. 29, 2020).
[45] K. Wang *et al.*, "Low-Cost and High-Performance Hard Carbon Anode Materials for Sodium-Ion Batteries," *ACS Omega*, vol. 2, no. 4, pp. 1687–1695, Apr. 2017, doi: 10.1021/acsomega.7b00259.
[46] P. Caussin, J. Nusinovici, and D. W. Beard, "Using Digitised X-Ray Powder Diffraction Scans as Input for a New Pc-At Search/Match Program," *Adv. X-Ray Anal.*, vol. 31, pp. 423–430, ed 1987, doi: 10.1154/S0376030800022254.
[47] S. Gražulis *et al.*, "Crystallography Open Database – an open-access collection of crystal structures," *J. Appl. Crystallogr.*, vol. 42, no. Pt 4, pp. 726–729, Aug. 2009, doi: 10.1107/S0021889809016690.
[48] A. Maetz, L. Delmotte, G. Moussa, J. Dentzer, S. Knopf, and C. M. Ghimbeu, "Facile and sustainable synthesis of nitrogen-doped polymer and carbon porous spheres," *Green Chem.*, vol. 19, no. 9, pp. 2266–2274, May 2017, doi: 10.1039/C7GC00684E.
[49] J. L. Figueiredo, M. F. R. Pereira, M. M. A. Freitas, and J. J. M. Órfão, "Modification of the surface chemistry of activated carbons," *Carbon*, vol. 37, no. 9, pp. 1379–1389, Jan. 1999, doi: 10.1016/S0008-6223(98)00333-9.
[50] A. Beda, C. Villevieille, P.-L. Taberna, P. Simon, and C. M. Ghimbeu, "Self-Supported Binder-Free Hard Carbon Electrodes for Sodium-Ion Batteries: Insights into the Sodium Storage Mechanisms," *J. Mater. Chem. A*, Feb. 2020, doi: 10.1039/C9TA13189B.
[51] C. Matei Ghimbeu, J. Górka, V. Simone, L. Simonin, S. Martinet, and C. Vix-Guterl, "Insights on the Na+ ion storage mechanism in hard carbon: Discrimination between the porosity, surface functional groups and defects," *Nano Energy*, vol. 44, pp. 327–335, Feb. 2018, doi: 10.1016/j.nanoen.2017.12.013.
[52] B. Zhang, C. M. Ghimbeu, C. Laberty, C. Vix-Guterl, and J.-M. Tarascon, "Correlation Between Microstructure and Na Storage Behavior in Hard Carbon," *Adv. Energy Mater.*, vol. 6, no. 1, p. 1501588, 2016, doi: 10.1002/aenm.201501588.
[53] E. Peled and S. Menkin, "Review—SEI: Past, Present and Future," *J. Electrochem. Soc.*, vol. 164, no. 7, pp. A1703–A1719, Jan. 2017, doi: 10.1149/2.1441707jes.
[54] A. Beda, P.-L. Taberna, P. Simon, and C. Matei Ghimbeu, "Hard carbons derived from green phenolic resins for Na-ion batteries," *Carbon*, vol. 139, pp. 248–257, Nov. 2018, doi: 10.1016/j.carbon.2018.06.036.
[55] S. Wang, L. Xia, L. Yu, L. Zhang, H. Wang, and X. W. (David) Lou, "Free-Standing Nitrogen-Doped Carbon Nanofiber Films: Integrated Electrodes for Sodium-Ion Batteries with Ultralong Cycle Life and Superior Rate Capability," *Adv. Energy Mater.*, vol. 6, no. 7, p. 1502217, 2016, doi: 10.1002/aenm.201502217.
[56] C. Bommier, T. W. Surta, M. Dolgos, and X. Ji, "New Mechanistic Insights on Na-Ion Storage in Nongraphitizable Carbon," *Nano Lett.*, vol. 15, no. 9, pp. 5888–5892, Sep. 2015, doi: 10.1021/acs.nanolett.5b01969.
[57] D. Saurel, B. Orayech, B. Xiao, D. Carriazo, X. Li, and T. Rojo, "From Charge Storage Mechanism to Performance: A Roadmap toward High Specific Energy Sodium-Ion Batteries through Carbon Anode Optimization," *Adv. Energy Mater.*, vol. 8, no. 17, p. 1703268, 2018, doi: 10.1002/aenm.201703268.
[58] N. Sun *et al.*, "Extended 'Adsorption–Insertion' Model: A New Insight into the Sodium Storage Mechanism of Hard Carbons," *Adv. Energy Mater.*, vol. 9, no. 32, p. 1901351, 2019, doi: 10.1002/aenm.201901351.
[59] S. Komaba *et al.*, "Electrochemical Na Insertion and Solid Electrolyte Interphase for Hard-Carbon Electrodes and Application to Na-Ion Batteries," *Adv. Funct. Mater.*, vol. 21, no. 20, pp. 3859–3867, 2011, doi: 10.1002/adfm.201100854.
[60] D. A. Stevens and J. R. Dahn, "An In Situ Small-Angle X-Ray Scattering Study of Sodium Insertion into a Nanoporous Carbon Anode Material within an Operating Electrochemical Cell," *J. Electrochem. Soc.*, vol. 147, no. 12, pp. 4428–4431, Dec. 2000, doi: 10.1149/1.1394081.
[61] V. Simone, A. Boulineau, A. de Geyer, D. Rouchon, L. Simonin, and S. Martinet, "Hard carbon derived from cellulose as anode for sodium ion batteries: Dependence of electrochemical properties on structure," *J. Energy Chem.*, vol. 25, no. 5, pp. 761–768, Sep. 2016, doi: 10.1016/j.jechem.2016.04.016.

[62] Y. Li, Y.-S. Hu, M.-M. Titirici, L. Chen, and X. Huang, “Hard Carbon Microtubes Made from Renewable Cotton as High-Performance Anode Material for Sodium-Ion Batteries,” *Adv. Energy Mater.*, vol. 6, no. 18, p. 1600659, Sep. 2016, doi: 10.1002/aenm.201600659.